Computational Mechanics (2023) 71:721–743
https://doi.org/10.1007/s00466-022-02258-8

ORIGINAL PAPER

Investigating shock wave propagation, evolution, and anisotropy using a moving window concurrent atomistic–continuum framework

Alexander S. Davis[1] · **Vinamra Agrawal**[1]

Received: 24 October 2022 / Accepted: 5 December 2022 / Published online: 20 January 2023

Abstract
Despite their success in microscale modeling of materials, atomistic methods are still limited by short time scales, small domain sizes, and high strain rates. Multiscale formulations can capture the continuum-level response of solids over longer runtimes, but using such schemes to model highly dynamic, nonlinear phenomena is very challenging and an active area of research. In this work, we develop novel techniques within the concurrent atomistic–continuum (CAC) multiscale framework to simulate shock wave propagation through a two-dimensional, single-crystal lattice. The technique is described in detail, and two moving window methods are incorporated to track the shock front through the domain and thus prevent spurious wave reflections at the atomistic–continuum interfaces. We compare our simulation results to analytical models as well as previous atomistic and CAC data and discuss the apparent effects of lattice orientation on the shock response of two materials. We then use the moving window techniques to perform parametric studies which analyze the shock front's structure. Finally, we compare the efficiency of our model to molecular dynamics simulations. This work showcases the framework's capability for simulating dynamic shock evolution over long runtimes and opens the door to more complex studies involving shock propagation through composites and alloys.

Keywords Concurrent atomistic–continuum · Shock waves · Multiscale modeling · Moving window · Molecular dynamics

1 Introduction

Shock waves are complex events which can induce catastrophic damage to materials through plastic deformation and spall fracture. As such, considerable effort has been devoted towards understanding shock propagation within solids at the continuum level [1,2]. However, a material's response to shock wave loading is linked to intricate behavior at the microscale. For example, in ductile metals, fracture caused by a shock wave impact is the direct result of dislocations and void nucleation within the material's microstructure [3–5]. Hence, it is imperative to understand shock wave propagation and evolution at the microscale in order to adequately predict material behavior at the macroscale.

Atomistic shock wave simulations have been performed over the past several decades primarily using a technique known as non-equilibrium Molecular Dynamics (NEMD). In these simulations, the shock is typically generated by an impact or with a moving piston and is then allowed to propagate through the domain [6]. Recent works have significantly increased the size and scope of NEMD frameworks to contain millions or sometimes billions of particles, and these formulations have been used to model events such as dislocation generation [7–10], twinning [11–13], void nucleation [14–16], and shock-induced spallation [17–21]. Unfortunately, NEMD techniques suffer from issues related to limited domain sizes and a large computational overhead which can cause artificial wave reflection and drastically restrict the total runtime [22]. In the past two decades, alternative atomistic techniques have been developed to counteract such issues, and some examples are the multiscale shock technique (MSST) [23,24], the uniaxial Hugoniostat [25,26], and the moving window method [27–29].

While modern atomistic techniques have greatly expanded our knowledge of shock wave behavior at the microscale, they nevertheless fail to capture the continuum-level response because the overall quantity of particles than can be integrated into the domain is restricted by computer architecture and limited computational resources. To overcome these

✉ Vinamra Agrawal
vza0013@auburn.edu

[1] Department of Aerospace Engineering, Auburn University, Auburn, AL, USA

issues, *concurrent multiscale* frameworks have been developed which preserve atomistic information around a small region of interest and populate the remainder of the domain with finite elements [30–34]. A primary concern of concurrent methods is ensuring numerical compatibility at the atomistic–continuum (A–C) interfaces in order to reduce spurious wave reflections and ghost forces. A variety of schemes have been established which attempt to solve this issue in different ways [35], and some examples include the Coupled Atomistic Discrete Dislocation (CADD) method [36], the Bridging Domain (BD) method [37], the Coupling of Length Scales (CLS) method [38], and the Quasicontinuum (QC) method [39]. Although methods such as these have had great success in material modeling, many of them still suffer from interface discrepancy due to a difference in material description and governing equations between the atomistic and continuum regions.

The Concurrent Atomistic–Continuum (CAC) method overcomes many of the A–C interface issues seen in other concurrent schemes by utilizing a unified multiscale framework whereby the governing equations from Atomistic Field Theory [40,41] are employed throughout the whole domain [42–51]. As a result, CAC has seen tremendous success over the past decade in modeling phenomena such as dislocations and grain boundaries [52,53] as well as passing high-frequency waves between the atomistic and continuum regions [49,54]. Recent work has even implemented an A-atom approach within CAC to perform large-scale simulations of multicomponent alloys [55], and research of dislocation evolution [56] as well as crystal plasticity [57] is ongoing. Unfortunately, the study of shock wave propagation using the CAC method has been limited due to the highly dynamic nature of such phenomena. While previous work has addressed this complication by incorporating moving window techniques into a CAC framework to track a nonlinear shock wave for long runtimes [58], this formulation only considered a 1D chain of particles and was thus limited in scope.

In the present work, we develop a multiscale framework using the CAC method to simulate long-time shock wave propagation through a two-dimensional lattice. Specifically, we utilize both the Hugoniot shock equations [1] as well as the nonlinear Eulerian thermoelastic shock equations [59] to analyze the well-known Riemann problem of an individual discontinuity traveling through a material. Furthermore, we enhance the moving window techniques first presented in [58] to track the shock over long simulation times and engineering-scale domains. Each method keeps the shock front in the middle of the atomistic region for the entire runtime, so the wave front never encounters the A–C interfaces. This allows us to model shock propagation for greater simulation times than traditional NEMD and multiscale methods and thus gain valuable information about the long-term, time-averaged material response to shock loading of two different face-centered cubic (FCC) ductile metals: Cu and Al.

This paper is organized as follows. Section 2 characterizes the shocks studied in the present work and elaborates on both the Hugoniot and Eulerian analytical models. Section 3 describes the framework's geometry and boundary conditions as well as presents the interatomic potential, thermostat, material parameters, and shock constants utilized in the simulations. Section 4 discusses the finite element formulation of CAC and its 2D implementation. Section 5 outlines both the shock propagation technique and the two moving window schemes used to track the shock front. Section 6 presents shock propagation results obtained with the conveyor technique and compares these to both analytical models to highlight the directional anisotropies in single crystals subject to shock loading. Section 7 uses the coarsen-refine technique to perform parametric studies related to the shock front's structure as well as showcases the efficiency of the current model compared to NEMD simulations. Finally, Sect. 8 concludes the paper and discusses ideas for future work.

2 Shock wave background

2.1 Problem statement

We consider a defect-free two-dimensional monatomic lattice compressed by an ideal longitudinal shock wave traveling in the x-direction. We mathematically characterize the shock front as a traveling discontinuity across which there is a jump in particle velocity (v), stress (σ), strain (ϵ), and temperature (θ). Material quantities behind the discontinuous shock front are denoted by the superscript $+$, and quantities in front of the shock front are denoted by the superscript $-$. Additionally, the notation $[\![\cdot]\!]$ represents the change in a certain quantity $(\cdot)$ across the discontinuity. During every simulation, particles ahead of the shock wave front have zero mean particle velocity, stress, and strain; and they remain at room temperature (295 K). Furthermore, the shock propagates at a natural velocity U_S along the surface of the primitive unit cell of an FCC lattice.

We utilize the parameters v, σ, ϵ, θ, and U_S in our two-dimensional CAC formulation to analyze long-time shock wave propagation over engineering-scale domains. In particular, we model the traditional Riemann problem of a single shock front with constant states on either side of the discontinuity (see Fig. 1). To calculate the aforementioned jump parameters and thus describe the macroscale shock response characterize the shock wave at the continuum level we use two different formulations which are discussed below.

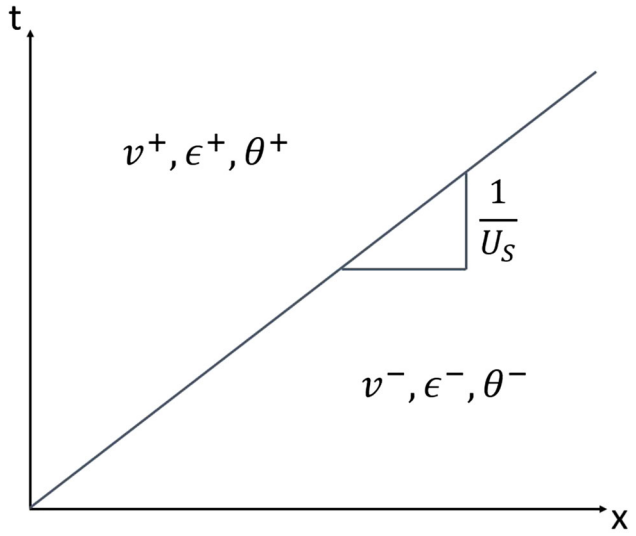

Fig. 1 Riemann problem of a shock with constant states behind and in front of the wave front [58]

2.2 Hugoniot shock equations

First, we simulate dynamic shock wave propagation and evolution using the conservation of momentum, continuity equation, Hugoniot equation of state (EOS), and a thermodynamic relationship derived from the shock Hugoniot and release isentrope. By applying the conservation of linear momentum and continuity of displacement across the discontinuous shock front and assuming uniaxial loading, we obtain the following standard one-dimensional shock wave jump equations [2]:

$$[\![\sigma]\!] + \rho U_s [\![v]\!] = 0 \tag{1}$$

$$[\![v]\!] + U_s [\![\epsilon]\!] = 0 \tag{2}$$

where ρ denotes the density of the material. To fully parameterize the system, we also employ an empirical linear relationship between shock velocity and particle velocity [1]:

$$U_s = C_0 + S[\![v]\!]. \tag{3}$$

In Eq. (3), C_0 is the sound velocity in the material at zero stress, and S is the slope of the shock velocity vs. particle velocity curve. We can use Eqs. (1), (2), and (3) to derive the following Hugoniot stress-strain relationship:

$$\sigma = \frac{\rho C_0^2 [\![\epsilon]\!]}{(1 + S[\![\epsilon]\!])^2} \tag{4}$$

where compression is positive in this paper. Eq. (4) is the standard Hugoniot EOS used in many simulations of shock waves through materials [29]. Finally, we calculate the rise in temperature across the shock front by solving the following ordinary differential equation [2]:

$$C_V \left(\frac{d\theta}{d\epsilon}\right)_H - \frac{\Gamma_1 \theta C_V}{1-\epsilon} = \frac{\epsilon}{2}\left(\frac{d\sigma}{d\epsilon}\right)_H - \frac{\sigma}{2} \tag{5}$$

where C_V is the volumetric specific heat capacity, and Γ_1 is the first-order Grüneisen parameter for the material.

2.3 Eulerian shock equations

We also characterize the propagating shock wave using the nonlinear Eulerian thermoelastic shock equations derived for anisotropic crystals in [59,60]. Nonlinear elastic constitutive models of material behavior which do not account for slippage and plasticity are generally idealizations because even small uniaxial compressive strains can cause ductile materials to reach the experimental Hugoniot elastic limit (HEL). However, such elastic formulations can be practically applied to defect-free atomistic and multiscale simulations of ductile solids since these systems may be shocked to finite strains over relatively short runtimes and small areas [60,61]. Furthermore, we note that nonlinear elastic models may be used to describe the finite compression of some strong crystals like diamond since the HEL of such materials is very large.

For an extensive derivation of the Eulerian formulation for shock waves, we refer the reader to [59]. Here, we merely present the relevant equations used in the current work. The particle velocity in the shocked material, shock propagation velocity, and temperature in the shocked material are given by the following respective equations:

$$v = \left\{\left(\frac{\hat{S}}{\rho}\right)\left[(1-2D) - (1-2D)^{3/2}\right]\right\}^{1/2} \tag{6}$$

$$U_S = v\left[1 - (1-2D)^{-1/2}\right]^{-1} \tag{7}$$

$$\theta = \frac{\partial \hat{U}}{\partial \eta} = \theta_0 \left(1 - \hat{\Gamma}_1 D - \frac{1}{2}\hat{\Gamma}_{11} D^2\right). \tag{8}$$

In Eqs. (6), (7), and (8), D is the Eulerian strain represented by the following expression:

$$D = \frac{1}{2}\left(1 - F^{-2}\right) = \frac{1}{2}\left[1 - \frac{1}{(1+\epsilon)^2}\right]. \tag{9}$$

Here, the term *Eulerian* means that the strain is a function of the inverse deformation gradient F. Hence, the strain tensor D assumes material coordinates rather than spatial coordinates, so it can be applied to the anisotropic shock simulations performed in this work [59]. Furthermore, $\hat{U}$ is the Eulerian fourth-order internal energy function as seen below [60]:

$$\hat{U} = \frac{1}{2}\hat{C}_{11}D^2 + \frac{1}{6}\hat{C}_{111}D^3 + \frac{1}{24}\hat{C}_{1111}D^4 - \theta_0\left(\hat{\Gamma}_1 D + \frac{1}{2}\hat{\Gamma}_{11}D^2 - 1\right)\eta \tag{10}$$

where $\hat{C}_{11}$, $\hat{C}_{111}$, and $\hat{C}_{1111}$ are the Eulerian second, third, and fourth-order elastic constants, $\hat{\Gamma}_1$ and $\hat{\Gamma}_{11}$ are the Eulerian first and second-order Grüneisen parameters, and $\eta = 0$ is the entropy ahead of the shock front. The elastic constants and Grüneisen parameters in an Eulerian setting are obtained from their non-Eulerian counterparts using the following relations [59,62,63]:

$$\hat{C}_{11} = C_{11} \tag{11}$$

$$\hat{C}_{111} = C_{111} + 12C_{11} \tag{12}$$

$$\hat{C}_{1111} = C_{1111} - 18C_{111} - 318C_{11} \tag{13}$$

$$\hat{\Gamma}_1 = \Gamma_1 \tag{14}$$

$$\hat{\Gamma}_{11} = \Gamma_{11} + 4\Gamma_1. \tag{15}$$

Finally, the conjugate stress $\hat{S}$ is represented by

$$\hat{S} = \frac{\partial \hat{U}}{\partial D} = C_{11}D + \frac{1}{2}\hat{C}_{111}D^2 + \left(\frac{1}{6}\hat{C}_{1111} - \theta_0\hat{\Gamma}_1 b_3\right)D^3 - \theta_0 D^4\left[\left(\hat{\Gamma}_1 b_4 + \hat{\Gamma}_{11}b_3\right) + \left(\hat{\Gamma}_1 b_5 + \hat{\Gamma}_{11}b_4\right)D\right] \tag{16}$$

where b_3, b_4, and b_5 are polynomials for entropy η generated across the shock front, and their expressions can be found in [59]. In each shock wave simulation, we use the fourth-order expression of Eqs. (6), (7), and (8).

2.4 'Elastic' shock waves

To legitimately utilize the shock equations from Sect. 2.3 as well as avoid intractability with the moving window techniques, we perform shock simulations with relatively small strains such that the resulting stresses are below the HEL of the material (see Appendix A.2). To maintain consistency, we refer to these as *elastic* shock waves in the present work. Elastic shock waves are often modeled in defect-free crystals with NEMD techniques to study a particular phenomenon, test a new framework, or validate a given potential [29,61,64], and their distinguishing characteristic is the lack of any permanent dislocations (inelastic deformation) behind the wave front. This is possible because the HEL is typically higher than what is seen in experimental settings [44], and the wave speed is still greater than the sound velocity in the material at the low strains. Modeling shock propagation with the CAC moving window framework using thermoelastic-viscoplastic models [65,66] is a worthy pursuit but would add an extra layer of complexity to the current model and is thus reserved for future studies.

3 Computational framework

3.1 Geometry and boundary conditions

We use our personal C++ code to develop, test, operate, and update the two-dimensional CAC framework used in this work, so we briefly discuss the formulation setup in this section.

The monatomic lattice is divided into three primary regions as seen in Fig. 2. The two coarse-scaled (continuum) regions are composed of rhombus elements, and the four particles which make up any particular element are classified as *nodes* in this paper. We choose rhombus elements because they align with the primitive unit cell of the FCC lattice (see Sect. 4.2) and thus facilitate a smooth transition between the fine-scaled and coarse-scaled regions. Specifically, the x-direction corresponds to the [112] lattice orientation while the y-direction corresponds to the $[\bar{1}10]$ lattice orientation. Since element connectivity is not required in CAC [42], each node is a member of only one element, and this greatly reduces the complexity of the finite element formulation. Furthermore, the edges of the grid in the continuum regions are "filled in" with particles which we refer to as *boundary atoms* in this work. This is done in order to facilitate periodic boundary conditions as shown in [67].

The two continuum regions border the central fine-scaled (atomistic) region on the left and right-hand side, and we classify the particles in this region as either *inner atoms* or just *atoms* in this paper. The "elements" in the fine-scaled region are reduced to their smallest possible configuration such that only four atoms constitute the entire area of each element. Hence, both the fine-scaled and coarse-scaled regions are technically made up of rhombuses with the only differences being the area and mass of their respective elements. As a consequence, one governing equation along with a single mass matrix is utilized for both regions, the interatomic potential is the only constitutive relation, and all force calculations are nonlocal [47]. Thus, the particles at the A–C interfaces ($x_{A,0}$ and $x_{A,F}$) have a direct communication with each other without creating ghost forces [50,67].

We note that to avoid introducing non-physical strains into the domain during shock simulations, semi-periodic boundary conditions are employed in the x-direction whereby the particles at the extreme ends of the lattice (x_0 and x_F) are neighbors with the nodes at the A–C interfaces ($x_{A,0}$ and $x_{A,F}$ respectively) [58]. Additionally, since the present work only considers uniaxial compression, we utilize periodic boundary conditions in the y-direction when modeling a longitudinal shock wave.

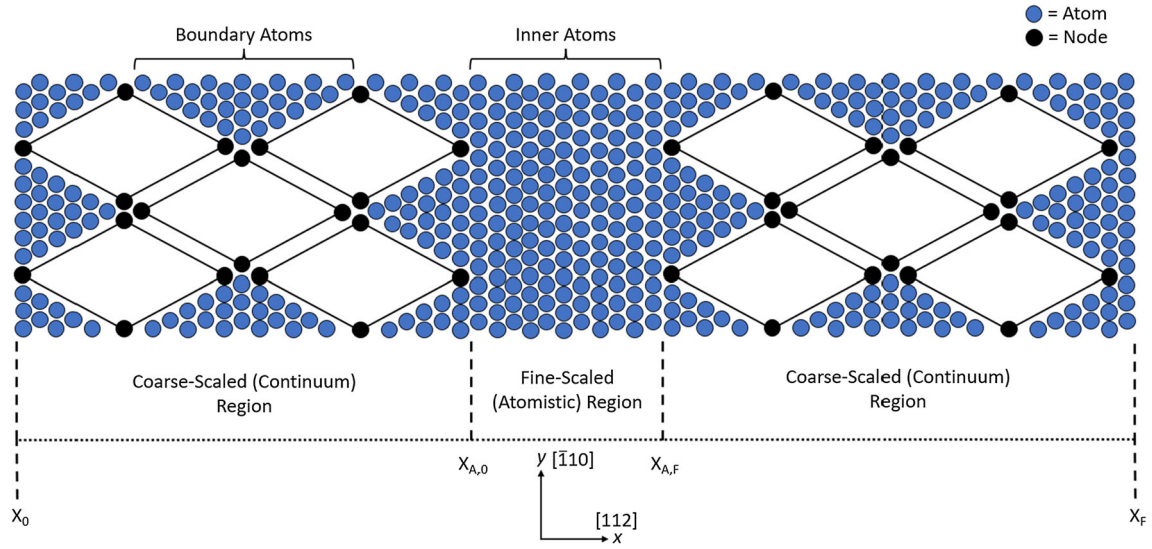

Fig. 2 Schematic of the two-dimensional CAC framework

3.2 Interatomic potential and material parameters

Since the parameters of complex multi-body potentials such as EAM are typically derived for 3D lattices, we use the modified Morse interatomic potential to find the integrand of the CAC internal force density (Eq. 19). Modified Morse only considers first nearest-neighbor interactions and has been shown to perform better than other pair potentials such as Lennard-Jones for FCC metals [29]. The equation for this potential function is as follows [68]:

$$\Pi(r_{ij}) = \frac{D_0}{2B-1}\left[\mathrm{e}^{-2\alpha\sqrt{B}(r_{ij}-r_0)} - 2B\mathrm{e}^{-\alpha(r_{ij}-r_0)/\sqrt{B}}\right] \tag{17}$$

where $r_{ij} = |\mathbf{x}_i - \mathbf{x}_j|$ is the magnitude of the displacement between particle i and j, and r_0 is the distance at which the potential reaches the minimum of the energy well (defined as the close-packed neighbor spacing). The modified Morse potential was derived from the standard Morse potential to more accurately capture the thermal expansion of materials [68]. We perform shock simulations with Cu and Al, and the parameters for these materials are given in Table 1.

3.3 Integration algorithm and thermostat

We integrate the CAC governing equation (Eq. 23) using the velocity Verlet algorithm with a time step of $\Delta t = 0.001$ ps to reduce numerical error. To apply temperature to the domain, we utilize the stochastic Langevin thermostat by discretizing the velocity Verlet algorithm according to the protocol from LAMMPS [69]. Since Langevin is a local thermostat, each particle has its own target temperature θ, and a different random variable is generated for each particle at every time step. For the compressive strains applied in this work, θ^+ has an upper boundary of ~ 450 K (θ^- is always set to 295 K).

3.4 Shock parameters

In Table 2, we present the empirical Hugoniot shock parameters as well as the second, third, and fourth-order elastic constants (in a normal and Eulerian setting) for both Cu and Al. The Hugoniot parameters are obtained from [70], the second and third-order elastic constants for Cu and Al are obtained from [71,72] respectively, and the fourth-order elastic constants are obtained from [60]. For these values, the temperature is assumed to be 295 K, C_0 is given in km/s, S is unitless, and the elastic constants are given in GPa. The Hugoniot parameters are derived for a shock wave propagating through a bulk, polycrystalline material. Furthermore, the elastic constants represent the pure-mode directions such that a planar shock impact results in an exclusively longitudinal component (along the [100] direction) with no transmitted shear stress, and hence the one-dimensional analysis is valid. We use these parameters as initial input in our shock simulations and compare the results from the CAC model to analytical and empirical data in Sect. 6.

4 CAC method

4.1 Finite element implementation

Here, we give a very brief overview of the finite element formulation of CAC, but for an extensive background of the technique and derivation of the relevant equations, we refer the reader to the many papers on CAC including the follow-

Table 1 Material constants and Morse parameters of two different FCC metals [68]

Element	Mass (u)	ρ_0 (g/cm^3)	Γ_1	r_0 (Å)	a (Å^{-1})	D_0 (eV)	B
Cu	63.55	8.96	1.97	2.5471	1.1857	0.5869	2.265
Al	26.98	2.70	2.17	2.8485	1.1611	0.3976	2.5

Table 2 Hugoniot and Eulerian shock parameters for Cu and Al ($\theta = 295$ K, C_0 in km/s, and $C_{\alpha\beta}$ in GPa)

Property	Cu [100]	Al [100]
C_0	3.94	5.33
S	1.49	1.34
C_{11}	166	107
C_{111}	− 1270	− 1080
$\hat{C}_{111}$	722	204
C_{1111}	11,900	25,000
$\hat{C}_{1111}$	2000	10,500

ing: [42,51,73,74]. CAC is based upon the mathematics of Atomistic Field Theory (AFT), and the governing equations of AFT have a similar form to the balance laws in continuum mechanics. Exploiting the definitions of internal force density and kinetic temperature derived in [75,76], we can recast the equation of linear momentum as follows [73]:

$$\rho^\alpha \ddot{\mathbf{u}}^\alpha(\mathbf{x}) = \mathbf{f}^\alpha_{int}(\mathbf{x}) + \mathbf{f}^\alpha(\mathbf{x}). \tag{18}$$

In Eq. (18), $\mathbf{u}^\alpha(\mathbf{x})$ is the displacement of the αth atom in the unit cell, $\rho^\alpha = m^\alpha/\Delta V$ is the mass density, m^α is the mass of the αth atom, ΔV is the volume of the unit cell, $\mathbf{f}^\alpha_{int}(\mathbf{x})$ is the internal force density, and $\mathbf{f}^\alpha(\mathbf{x})$ is the force density from external forces and temperature. The two terms on right side of Eq. (18) are represented as follows:

$$\mathbf{f}^\alpha_{int}(\mathbf{x}) = \int_{\Omega(\mathbf{x}')} \sum_{\beta=1}^{N_a} \mathbf{f}\left[\mathbf{u}^\alpha(\mathbf{x}) - \mathbf{u}^\beta(\mathbf{x}')\right] d\mathbf{x}' \tag{19}$$

$$\mathbf{f}^\alpha(\mathbf{x}) = \mathbf{f}^\alpha_{ext}(\mathbf{x}) - \frac{m^\alpha k_B}{M\Delta V}\nabla_{\mathbf{x}}\theta^\alpha \tag{20}$$

where $\mathbf{f}^\alpha_{ext}(\mathbf{x})$ is the external force density, M is the total mass of atoms within a unit cell, and θ^α is the kinetic temperature. We note that since the internal force density is a nonlocal function of the various distances between neighboring particles, it can be determined solely from the interatomic potential [77].

We employ the finite element method to calculate the numerical solution of Eq. (18). In particular, we populate the domain with finite elements such that every element consists of an assemblage of unit cells, and each nodal location represents a unit cell which is itself made up of particles. As a result, CAC provides a two-level description of crystals and follows the solid state physics model whereby the material is continuous at the macroscale but discrete at the microscale. We use interpolation within each element in the domain to approximate the displacement field with the following expression [42]:

$$\hat{\mathbf{u}}^\alpha(\mathbf{x}) = \mathbf{\Phi}_\xi(\mathbf{x})\mathbf{U}^\alpha_\xi. \tag{21}$$

In Eq. (21), $\hat{\mathbf{u}}^\alpha(\mathbf{x})$ is the displacement field for the αth atom in an element, $\mathbf{\Phi}_\xi(\mathbf{x})$ is the shape function, and $\mathbf{U}^\alpha_\xi$ is the displacement of the αth atom within the ξth node of the element. Here, $\xi = 1, 2, ..., n$ where n equals the total number of nodes in the element (four in this work).

Applying the method of weighted residuals, we arrive at the weak form of the governing equation by multiplying Eq. (18) with a weight function $\mathbf{\Phi}_\eta(\mathbf{x})$ and integrating over the whole system:

$$\begin{aligned}\int_{\Omega(\mathbf{x})} \left[\rho^\alpha \mathbf{\Phi}_\eta(\mathbf{x})\ddot{\mathbf{u}}^\alpha(\mathbf{x})\right] d\mathbf{x} \\ = \int_{\Omega(\mathbf{x})} \left[\mathbf{\Phi}_\eta(\mathbf{x})\mathbf{f}^\alpha_{int}(\mathbf{x})\right] d\mathbf{x} + \int_{\Omega(\mathbf{x})} \left[\mathbf{\Phi}_\eta(\mathbf{x})\mathbf{f}^\alpha(\mathbf{x})\right] d\mathbf{x}.\end{aligned} \tag{22}$$

Specifically, the Galerkin method is used to obtain the above expression, so the weight function $\mathbf{\Phi}_\eta(\mathbf{x})$ equals the shape function $\mathbf{\Phi}_\xi(\mathbf{x})$ in this case. Substituting Eqs. (19), (20), and (21) into Eq. (22), we arrive at the following CAC governing equation:

$$\mathbf{M}^\alpha \ddot{\mathbf{U}}^\alpha_\xi = \mathbf{F}^\alpha_{int} + \mathbf{F}^\alpha \tag{23}$$

where $\mathbf{F}^\alpha$ is the third term in Eq. (22), and $\mathbf{M}^\alpha$ and $\mathbf{F}^\alpha_{int}$ are given as

$$\mathbf{M}^\alpha = \int_{\Omega(\mathbf{x})} \left[\rho^\alpha \mathbf{\Phi}_\eta(\mathbf{x})\mathbf{\Phi}_\xi(\mathbf{x})\right] d\mathbf{x} \tag{24}$$

$$\mathbf{F}^\alpha_{int} = \int_{\Omega(\mathbf{x})} \mathbf{\Phi}_\eta(\mathbf{x}) \int_{\Omega(\mathbf{x}')} \sum_{\beta=1}^{N_a} \mathbf{f}\left[\mathbf{\Phi}_\xi(\mathbf{x})\mathbf{U}^\alpha_\xi - \mathbf{\Phi}_\xi(\mathbf{x}')\mathbf{U}^\beta_\xi\right] d\mathbf{x}' d\mathbf{x}. \tag{25}$$

In this work, we use the row-sum method to approximate the inertial term (Eq. 24) with the lumped mass matrix derived in Appendix B.1. Additionally, there are no external forces, and we apply temperature using a thermostat as in [45,49]. Finally, we calculate the computationally expensive internal force density $\mathbf{F}^\alpha_{int}$ numerically using Gaussian integration as discussed in Appendix B.2.

The finite element formulation reviewed in this section eliminates most of the degrees of freedom in the coarse-scaled regions of the CAC domain. For critical regions where atomistic behavior is required, the smallest mesh is used such

that each rhombus "element" consists exclusively of four atoms with no additional lattice points. Thus, CAC builds upon AFT to produce a unified framework between the fine-scaled and coarse-scaled regions. A unique feature of CAC is that in the finite element implementation, element connectivity is not required because the nonlocal interatomic force field is the only constitutive relation [42]. This is similar to aspects of the cohesive zone model [78] and greatly simplifies the implementation of both the mass matrix as well as the force calculations.

4.2 Two-dimensional formulation

Rhombohedral elements are utilized within the CAC formulation to replicate the primitive unit cell of a monocrystalline lattice (FCC in the present work). A sketch of this can be seen in Fig. 3a, where we observe the primitive unit cell (blue lines) within the broader FCC crystal structure. Furthermore, the shaded region represents the two-dimensional atomic plane used in our formulation whereby rhombus elements are incorporated throughout the domain. Since the same constitutive relation is used both within elements as well as between elements, dislocations and cracks emerge naturally through the separation of finite elements [42]. This is a direct result of the CAC governing equations, and it allows such defects to pass smoothly across the A–C interfaces without deforming individual elements. As a result, some mesh sensitivity may be introduced into simulations with very high strains whereby different grid resolutions alter the convergence of the solution.

A schematic of the two-dimensional rhombus element can be seen in Fig. 3b. Here, the black circles represent the four nodes where the governing equations are applied, and the grey circles represent the lattice points which serve as nodal neighbors and thus aid in the force calculations. For monatomic crystals, each nodal location (unit cell) only contains one atom, and the positions of the lattice points are interpolated using Eq. (21) throughout the element. We emphasize that the lattice points are excluded from the Verlet algorithm. Finally, since no external forces are applied in this work, the governing equations from Sect. 4.1 reduce to the following:

$$\mathbf{M}\ddot{\mathbf{U}} - \mathbf{F}^{int} = \mathbf{0} \tag{26}$$

where the terms $\mathbf{M}$ and $\mathbf{F}^{int}$ are given as

$$\mathbf{M} = \int_{\Omega(\mathbf{x})} [\rho \mathbf{\Phi}(\mathbf{x}) \mathbf{\Phi}(\mathbf{x})]\, d\mathbf{x} \tag{27}$$

$$\begin{aligned} \mathbf{F}^{int} &= \int_{\Omega(\mathbf{x})} \mathbf{\Phi}(\mathbf{x}) \int_{\Omega(\mathbf{x}')} \sum_{j=1}^{n_\alpha} \mathbf{f}\left[\mathbf{\Phi}(\mathbf{x})\mathbf{U}_i - \mathbf{\Phi}(\mathbf{x}')\mathbf{U}_j\right] d\mathbf{x}' d\mathbf{x} \\ &= \int_{\Omega(\mathbf{x})} \mathbf{\Phi}(\mathbf{x}) \mathbf{f}^{int}(\mathbf{x}) d\mathbf{x}. \end{aligned} \tag{28}$$

In Eq. (26), $\mathbf{M}$ is the mass matrix, and Appendix B.1 provides a full derivation of this term. In brief, we utilize the lumped mass matrix approach in the present formulation which effectively reduces $\mathbf{M}$ to the following expression for each element:

$$\mathbf{M} = \frac{m N_{ppe}}{N_{npe}} \tag{29}$$

where m is the atomic mass, N_{ppe} is the number of particles per element (including lattice points), and N_{npe} is the number of nodes per element [67].

The terms $\ddot{\mathbf{U}}$ and $\mathbf{F}^{int}$ are the respective accelerations and internal forces for each atom/node in the lattice, and n_α represents the total number of neighbors of particle i within a specified cutoff radius. Furthermore, the local force $\mathbf{f}^{int}(\mathbf{x})$ on particle i at position $\mathbf{x}$ is obtained exclusively from the interatomic potential through relative displacements of particles, and the total force is obtained through Gaussian quadrature rules (see Appendix B.2). We note that the surrounding lattice points act as atomic neighbors when calculating the force $\mathbf{f}^{int}(\mathbf{x})$ of a node in the continuum regions, whereas in the fine-scaled region, atomic neighbors are merely other atoms.

5 Shock propagation technique

5.1 Shock initialization

For each simulation, the shock wave is characterized using either the Hugoniot (Sect. 2.2) or Eulerian (Sect. 2.3) governing equations, and the shock front is achieved by dividing the grid from Fig. 2 into different regions as seen in Fig. 4. The boundary particles within each continuum domain (red circles) constitute the *thermostat regions* (TRs) and are categorized as "damped" atoms since they apply a constant temperature to the lattice through the Langevin thermostat. Furthermore, a narrow band of inner atoms at each A–C interface are also damped to ensure that the *window region* (WR) made up of "undamped" atoms (blue circles) achieves the correct canonical ensemble [58]. We note that as in [79], the nodes (black circles) are left undamped to prevent spurious behavior within each element. The shock wave front (SWF) starts at the midpoint of the WR and travels to the right along the positive x-direction with a speed of U_S. We delineate material to the right of the SWF as the unshocked region and material to the left of the SWF as the shocked region.

To initialize the shock, we assign a final strain ϵ^+ to the shocked region and use either Eqs. (2) and (3) for the Hugoniot formulation or Eqs. (6) and (7) for the Eulerian formulation to calculate the mean particle velocity v^+ and SWF velocity U_S. The Hugoniot parameters C_0 and S as well as the elastic constants C_{11}, $\hat{C}_{111}$, and $\hat{C}_{1111}$ are initially assigned

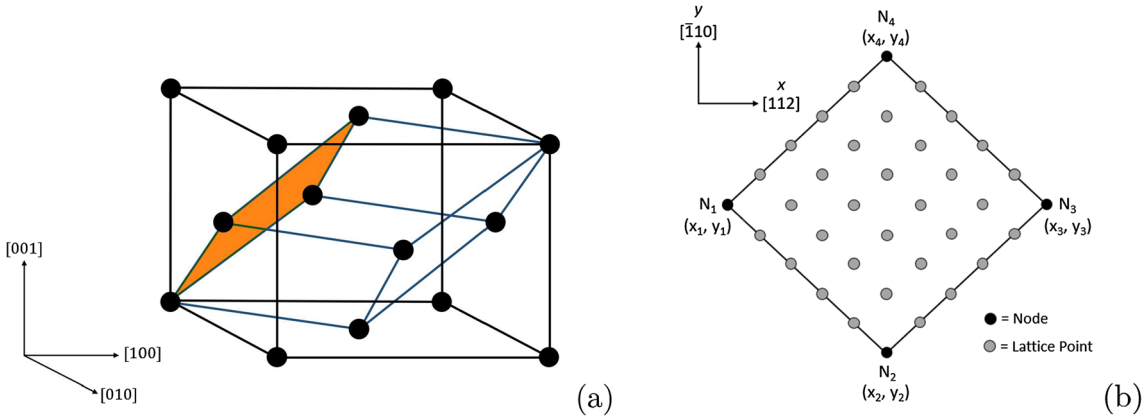

Fig. 3 **a** Rhombohedral element constituting the primitive unit cell (blue lines) of an FCC lattice. The shaded region represents the two-dimensional rhombus element utilized in the present formulation. **b** Schematic of the two-dimensional rhombus element

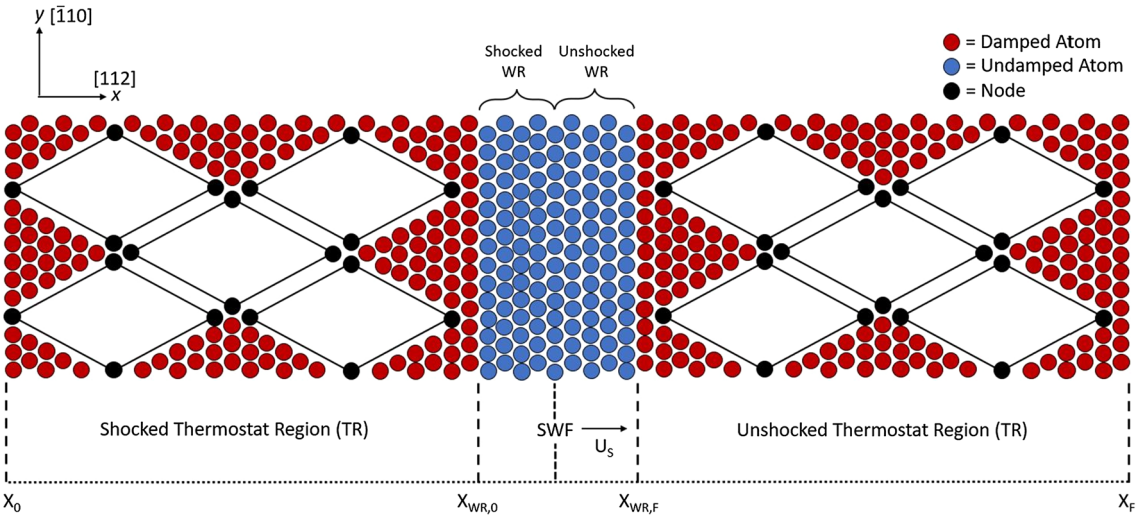

Fig. 4 CAC geometry used for shock wave simulations. Here, the red circles represent damped atoms, the blue circles represent undamped atoms, and the black circles represent nodes

their literature values given in Table 2. The particle velocity v^+ is the new equilibrium velocity for the shocked region, and the strain ϵ^+ causes the lattice to compress uniaxially such that particles behind the SWF obey the Cauchy-Born rule. As a result, the shocked region achieves its final state and the SWF starts to propagate forward beginning in the middle of the WR. The temperature θ^+ calculated from either Eq. (5) or (8) is applied to the shocked TR, and each TR is far enough away from the non-equilibrium SWF to be considered within a region of "local" equilibrium. Hence, we can legitimately apply the Langevin thermostat to the strained portion of the domain [25].

In this work, we overcome the runtime-limiting obstacle of boundary reflections present in traditional NEMD shock wave simulations by incorporating two moving window techniques into the multiscale framework. The first technique, known as the *conveyor* method, draws inspiration from the moving boundary conditions utilized in [80,81] to simulate dynamic crack propagation as well as the atomic insertion scheme from [27,28] to model piston-driven shocks. The second technique, known as the *coarsen-refine* method, has similarities to mesh refinement schemes used in finite element [82,83] as well as atomistic–continuum [47,84,85] frameworks. Both techniques serve to track the propagating shock front over engineering length scales and time frames by eliminating shock-boundary reflections, and a description of each can be found in the following sections.

5.2 Conveyor method

Figure 5 provides a schematic of the conveyor technique for the two-dimensional CAC framework. This technique is similar to the scheme found in [58] for one dimension, but there are more intricacies and complexities associated with the higher-dimensional lattice. After the SWF has traveled one lattice spacing (a_{lat}) along the positive x-direction from the

center of the WR, the initial position, displacement, velocity, and acceleration of particles in the first two columns of the grid are set equal to the parameters of their rightmost neighbors within the same row. The neighbors may be either boundary atoms, nodes, or lattice points, but if they are lattice points, the Verlet parameters are first interpolated as discussed in Sect. 4.1. Effectively, the parameters of particles within the first two columns of the lattice are removed from the simulation as is noted in the figure by the leftmost arrow.

This process continues throughout the entire domain from the beginning of the shocked region to the end of the unshocked region, and we note that only the initial position of lattice points are updated since their displacements, velocities, and accelerations are interpolated during the integration algorithm. Particles in the final column of the domain (denoted by the gold and orange circles in Fig. 5) are given new initial x-positions which are one lattice spacing greater than their current initial x-positions, and their y-positions remain the same. Furthermore, their displacements, velocities, and accelerations are all set equal to zero, and the Langevin thermostat dampens any energy fluctuations generated near x_F as in [28]. This conveyor mechanism occurs with a frequency of $\tau^{-1} = U_S/a_{lat}$, and if the simulated and analytical shock velocities are the same, the SWF will remain stationary in the middle of the WR for the entire runtime. The resulting time resolution of a_{lat}/U_S is thus optimized for the given shock propagation velocity, but higher time resolutions are achievable depending on the speed of the phenomenon in question.

5.3 Coarsen-refine method

A schematic of the coarsen-refine method can be seen in Fig. 6, and again it is similar in principle to the 1D technique from [58]. Here, after the SWF has traveled a distance equal to the length of the element diagonal (e_{diag}) plus the lattice spacing divided by two, the moving window mechanism begins whereby material in the shocked continuum region gets coarsened and material in the unshocked continuum region gets refined. In the shocked region, coarsening is achieved by transforming the relevant particles into nodes and lattice points such that new elements appear in the previous atomic locations. On the other hand, in the unshocked region, refinement takes place by changing nodes and lattice points into fine-scaled particles through both parameter re-assignment and linear interpolation—similar to what is done with the conveyor technique. This procedure effectively transmits the fine-scaled region forward to the new SWF location as seen in Fig. 6.

After this process completes, undamped particles at the A–C interfaces in the shocked material are redefined as damped particles and vice versa for particles in the unshocked material. Furthermore, the mass matrix is modified to exhibit the new mass distribution within the lattice. This technique occurs iteratively with a frequency of $\tau^{-1} = U_S/\frac{1}{2}\left(e_{diag} + a_{lat}\right)$, and the integer time counter n is increased by one each time the mechanism terminates (as shown in Fig. 6). When utilizing the coarsen-refine method, the entire two-dimensional grid remains stationary and merely the location of the fine-scaled region is shifted. As a result, most of the domain can be populated with finite elements while a comparatively small section of atoms track the propagating shock wave through the lattice. This technique thus ultimately endeavors to balance total efficiency and total accuracy of nonlinear shock wave modeling.

6 Elastic anisotropy: crystal orientation dependence of shock propagation response

In this section, we elaborate on the shock velocity and longitudinal stress results obtained with both the Hugoniot and Eulerian formulations and discuss how they relate to the directional anisotropy of materials subject to shock impact. Recent NEMD works have studied shock propagation along different lattice directions of single crystals and observed a significant orientation dependence on the material's shock response [86–89]. This phenomenon has also been documented for elastic shock waves in small-scale, atomistic domains [29,61]. Interestingly, large-scale experimental studies have not shown the same orientation dependence of shock parameters [90], but this may be due to the fact that bulk crystals naturally have more defects than what can be feasibly represented using atomistic techniques [88]. The present work provides a unique insight on this phenomenon because the CAC domain is modeled after the primitive unit cell of an FCC lattice and thus promotes a smooth transition between the atomistic and continuum regions. Hence, the shock travels along the [112] longitudinal direction, and the $\left[\bar{1}10\right]$ direction is transverse to the direction of propagation. To the authors' knowledge, this is one of the first studies to analyze shock evolution along this particular orientation.

6.1 Simulation specifications

The results in this section are obtained from shock wave simulations performed with the *conveyor* moving window technique using the CAC domain described in Fig. 4. For every simulation, the left and right coarse-scaled regions each contain 250 particle columns for a total length of $250a_{lat}$, and each element diagonal has a length of $8a_{lat}$. Furthermore, the fine-scaled region contains 2500 particle columns, and the length of each element diagonal is merely the lattice spac-

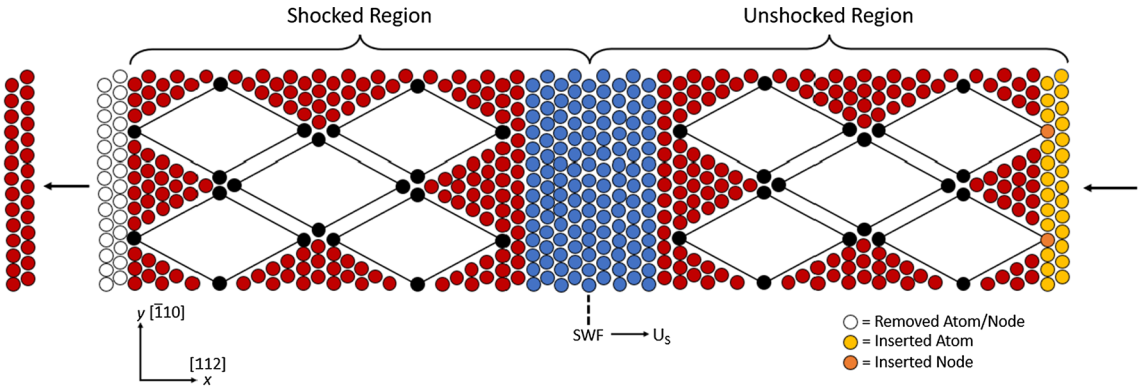

Fig. 5 Schematic of the moving window *conveyor* technique for the 2D CAC framework. The white circles represent removed particle locations while the gold/orange circles represent inserted particle locations

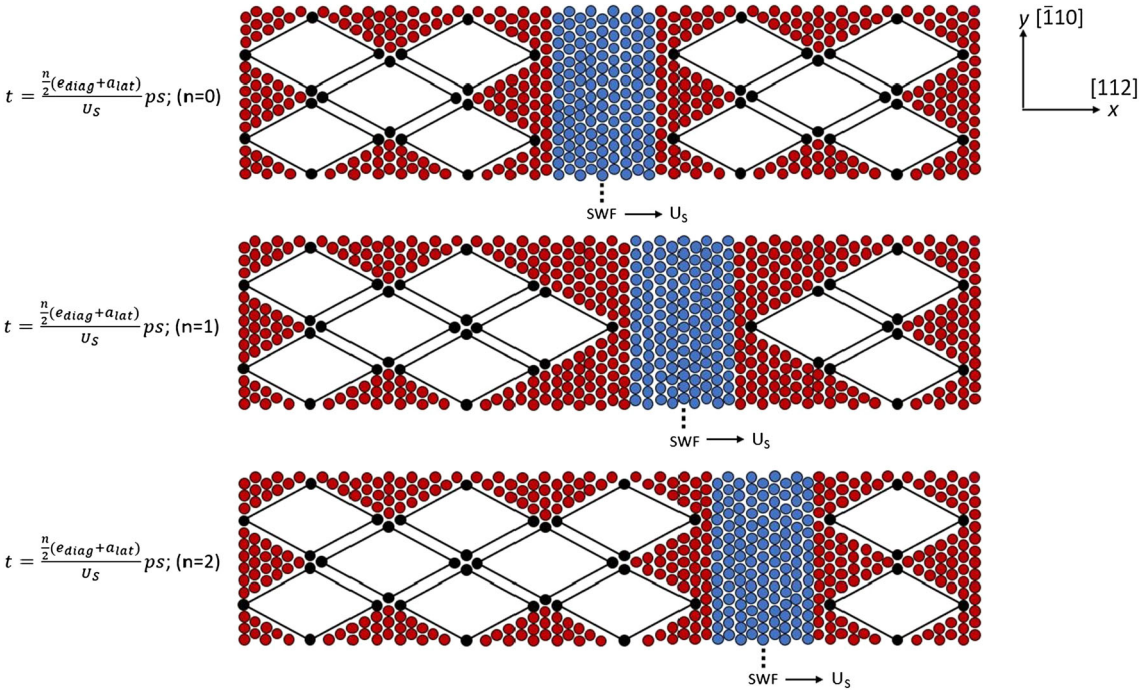

Fig. 6 Schematic of the moving window *coarsen-refine* technique for the 2D CAC framework

ing (a_{lat}). Additionally, each atomistic TR band contains 20 columns to ensure that the WR reaches the desired temperature [79]. Simulations are conducted for compressive strains (ϵ^+) ranging from 1% to 9% and 1% to 8% for Cu and Al respectively (see Appendix A.2), and the total runtime is 2 ns. A velocity profile of the two-dimensional shocked lattice can be seen in Fig. 7a. Specifically, we track the SWF over time in MATLAB by taking a column average of the particle velocities as shown in Fig. 7b.

6.2 Shock velocity results

Shock velocity results obtained for both Hugoniot and Eulerian theory can be seen in Figs. 8 and 9 respectively. Specifically, Fig. 8 displays the shock velocity vs. particle velocity data (as well as the derived Hugoniot equations) of four different sets of simulations using both (a) Cu and (b) Al. Here, the blue line represents the polycrystalline Hugoniot calculated in [70], and the green data points are the average velocity results for shocks propagating through the standard CAC domain. As a comparison, we also invert the lattice such that the $[\bar{1}10]$ orientation lies along the x-direction, and the [112] orientation lies along the y-direction, and these results are given by the red data points. As in Appendix A.2, we performed stress vs. strain studies for this inverted lattice and found yielding to occur at 9% strain for Cu and 8% strain for Al, so we maintain ϵ^+ values below these elastic limits when simulating shocks along the $[\bar{1}10]$ direction. Finally, we also

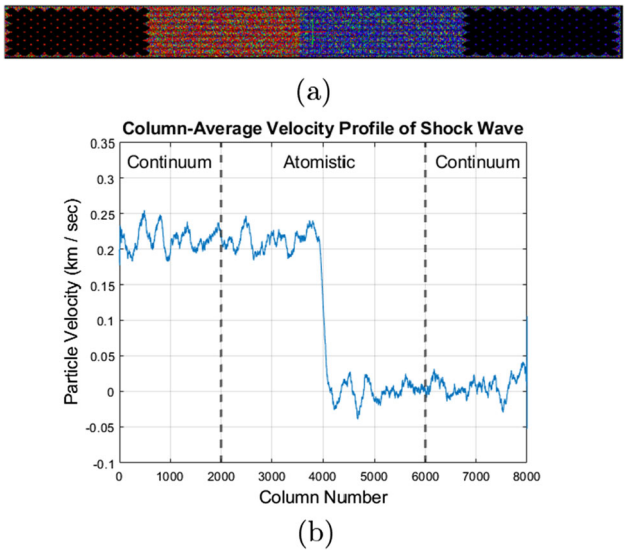

Fig. 7 Velocity profiles of the propagating shock in the CAC framework. **a** SWF in the two-dimensional grid (not to scale); **b** SWF obtained from averaging the column velocities of the lattice

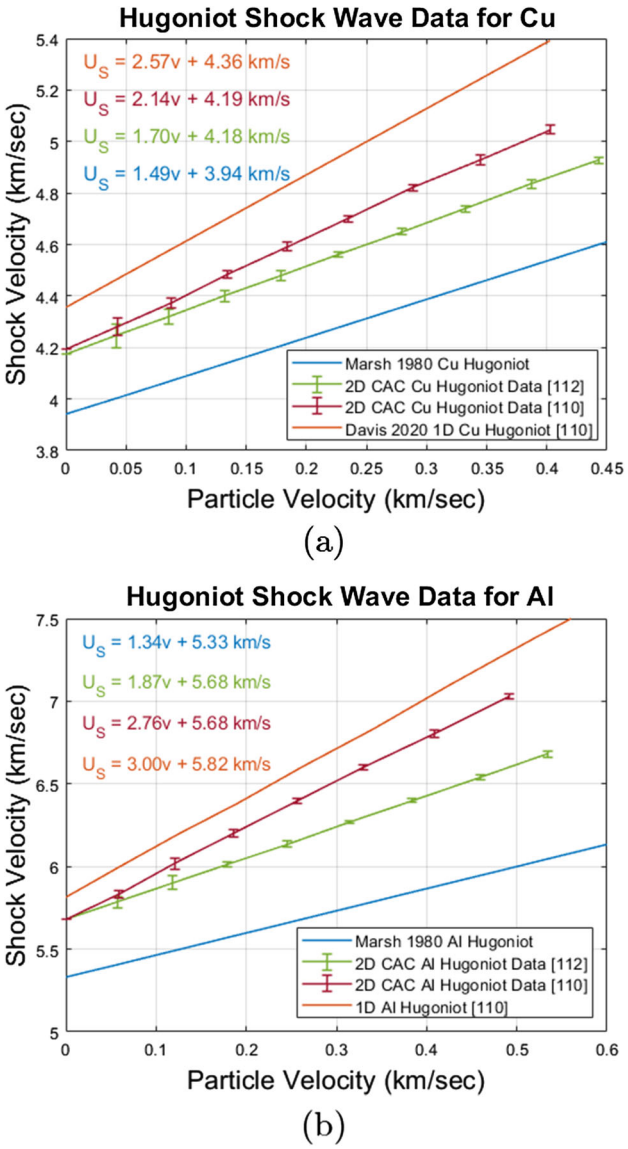

Fig. 8 Hugoniot shock wave results for both **a** Cu and **b** Al. The polycrystalline shock Hugoniot obtained from [70] is shown in blue. Two-dimensional CAC Hugoniot data obtained for shocks propagating along the [112] and $[\bar{1}10]$ lattice directions are shown in green and red respectively. One-dimensional shock Hugoniots are given in orange. The Cu Hugoniot comes from [29], and the Al Hugoniot is calculated in the present work

present one-dimensional atomistic shock data obtained from [29] for Cu and calculated in this work for Al.

The data and associated Hugoniot equations in Fig. 8 clearly show the dependency of a shock's propagation velocity on the given lattice orientation. In particular, both of the two-dimensional CAC Hugoniots have C_0 and S values which are greater than the standard polycrystalline Hugoniot. This is most likely due to the fact that the FCC primitive unit cell is rhombohedral instead of cubic, so the entire CAC lattice is more compressed than a traditional structured FCC grid. This causes the particles in the domain to be more compact which results in larger forces from the interatomic potential and hence higher shock velocities. Additionally, the polycrystalline Hugoniot data are fitted to strong shock waves for which yielding reduces the effects of the shear modulus. Hence, we would anticipate the shocks from [70] to be slower than the elastic CAC shocks since shear stress is limited to plastic yield strength. Next, as expected, the inverted CAC lattice produces slightly higher shock velocities than the lattice from Fig. 4 since the $[\bar{1}10]$ lattice spacing is shorter than the [112] spacing. Finally, the one-dimensional shock velocities are greater than the those from the two-dimensional simulations due to the lack of any transverse motion which naturally dampens the shock speed. Instead, the 1D results are comparable to plane-plane collisions in a bulk lattice [91].

We observe a similar phenomenon for the Eulerian results in Fig. 9 where we now plot average shock velocity vs. applied strain. Here, the green and red data points are from the same types of 2D simulations as those from Fig. 8. However, the blue line now represents the analytical results from fourth-order Eulerian theory, and the orange data points are 1D CAC shock results obtained from [58]. Since we utilize elastic constants obtained for shocks propagating along the [100] direction and the CAC formulation analyzes shocks along the [112] and $[\bar{1}10]$ directions, elastic anisotropy in the crystal lattice is a major reason why the results from the various models differ.

As seen previously, the 1D shock velocities are slightly greater than the 2D velocities from the present study, and the inverted CAC lattice has a higher slope than the standard CAC lattice. For Cu, the shock velocities predicted at

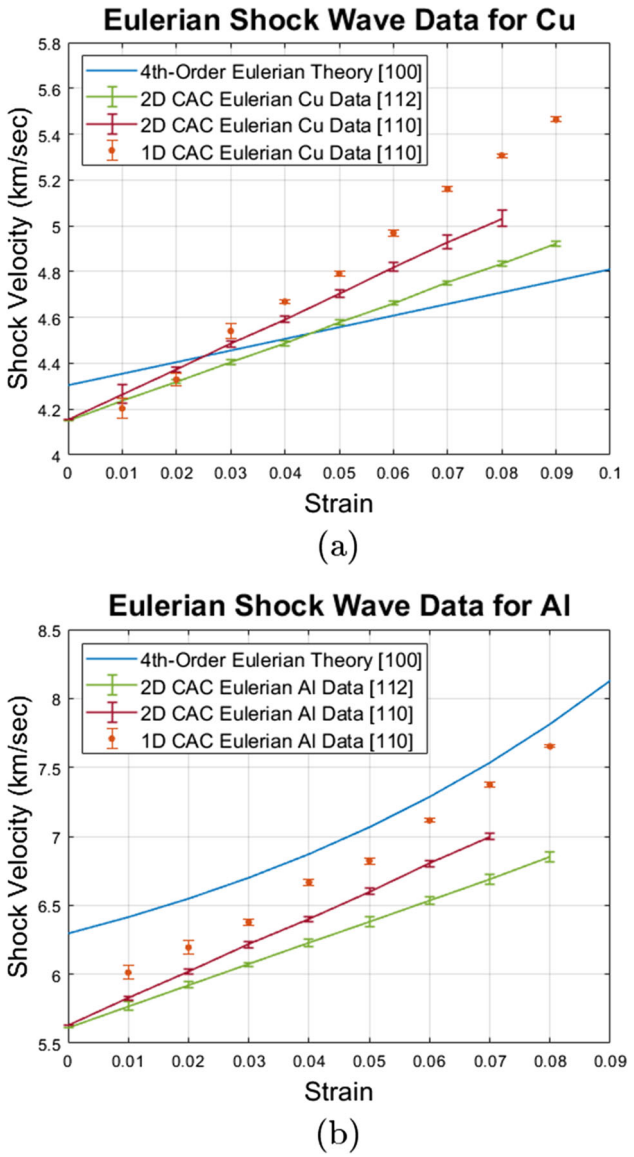

Fig. 9 Eulerian shock results for both **a** Cu and **b** Al. The blue line represents velocities obtained from fourth-order Eulerian theory. Two-dimensional CAC data obtained for shocks propagating along the [112] and $[\bar{1}10]$ lattice directions are shown in green and red respectively. One-dimensional CAC data obtained from [58] are in orange

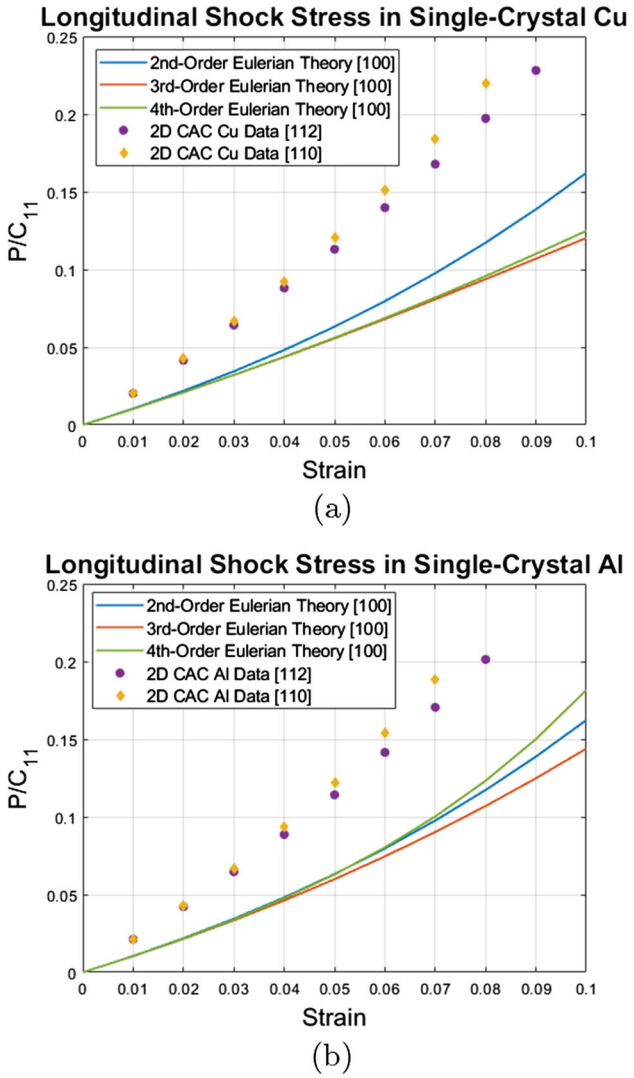

Fig. 10 Longitudinal stress data for both **a** Cu and **b** Al. The blue, orange, and green lines represent the [100] results from 2nd, 3rd, and 4th-order Eulerian theory respectively. The purple circles and gold diamonds represent the [112] and $[\bar{1}10]$ CAC data respectively

higher strains by Eulerian theory are indeed lower than the 2D and 1D CAC results, but this is not the case for Al. The reason for the anomalous results with Al is not necessarily clear, but it could be due to the fact that the third- and fourth-order elastic constants are not always measurable to high accuracy, so uncertainties in their values would lead to uncertainty in the results predicted by fourth-order Eulerian theory. Nonetheless, we observe qualitative compatibility between the Hugoniot and Eulerian formulations which gives us confidence that the current CAC framework produces accurate results and can thus be reliably used to measure the response of materials to shock propagation along various lattice directions.

6.3 Longitudinal stress results

To supplement the anisotropic shock velocity results from Sect. 6.2, we perform longitudinal stress vs. strain studies using the shocked data for both Cu and Al, and these results can be seen in Fig. 10. Specifically, we calculate the time-averaged virial (thermodynamic) stress (σ_{xx}) in the shocked region using Eq. (A1), and we relate the Cauchy stress (P_{xx}) to the virial stress as follows [61]:

$$P_{xx} = (1 - \epsilon)\sigma_{xx} \tag{30}$$

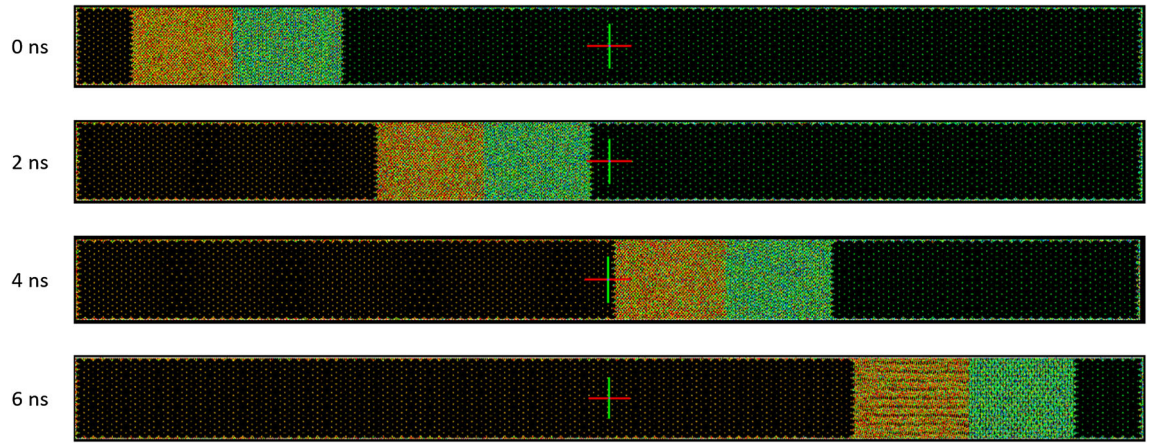

Fig. 11 Shock simulation using the coarsen-refine moving window technique

where we note that compressive stress/strain is considered positive.

Figure 10 shows the shock stress P_{xx} normalized by the second-order elastic constant C_{11} as a function of the applied strain. The data from Hugoniot and Eulerian theory were practically identical, so without loss of generality, we only exhibit the Eulerian results. The [100] second, third, and fourth-order Eulerian models are represented by the blue, orange, and green lines respectively, while the [112] and $[\bar{1}10]$ shock stress data are represented by the purple circles and gold diamonds respectively. As in Sect. 6.2, we clearly observe the orientation dependence and elastic anisotropy of the shock stress as the CAC data is significantly higher than that predicted by the various Eulerian models for shocks along the [100] direction. Furthermore, the $[\bar{1}10]$ CAC simulations produced shock stresses which were slightly higher than those from the [112] simulations. Again, this is primarily due to the higher compression velocities caused by the larger 'compactness' of CAC domains. This anisotropic stress data is congruent with a previous work which analyzed elastic shocks along various lattice directions using a number of different potential functions [61].

7 Results with the coarsen-refine method and formulation efficiency

Without loss of generality, we only reference data from Eulerian theory in this section as both shock models gave similar quantitative results.

7.1 Coarsen-refine simulations

In Fig. 11, we present results from a shock wave simulation performed using the *coarsen-refine* technique over 6 ns. Here, we can observe the atomistic portion of the domain successfully follow the evolving shock front throughout the CAC framework with no spurious wave behavior at the A–C interfaces. Due the elastic nature of the shock as discussed in Sect. 2.4, no dislocations are present to the left of the wave front, but we do see the shocked material maintain the mean particle velocity of v^+ for the entire runtime. These results are in contrast to those performed using the conveyor technique because now the SWF may travel through the entire CAC domain while staying within the fine-scaled region. Although previous work has used mesh refinement to study phenomena within both finite-element [82] and multiscale [47,84,85] schemes, utilizing simultaneous refine/coarsen techniques to study dynamic, high-temperature phenomena is still a challenging area of research [58]. Thus, the present formulation provides a novel means for tracking propagating shocks over long runtimes, and may be used to research even more complex lattice structures in the future such as nanoscale composites or high-entropy alloys.

7.2 Shock structure and planarity

We now use the coarsen-refine simulations to analyze the shock front's spatial width over 5 ns, and the results for $\epsilon^+ = -0.06$ can be seen in Fig. 12. As a comparison, we also show the 1D CAC results from [58]. Unlike the 1D data, the present work shows a clear steadiness in the shock wave behavior as evidenced by the fact that the shock width remains constant throughout the simulation with very little deviation from the mean. We also do not observe a significant change in the shock front's planarity throughout the simulation's duration. Finally, similar results were found for both Cu and Al over the range of strains studied with the present formulation. Clearly, for shock waves modeled at the microscale, the ability of particles to oscillate transversely

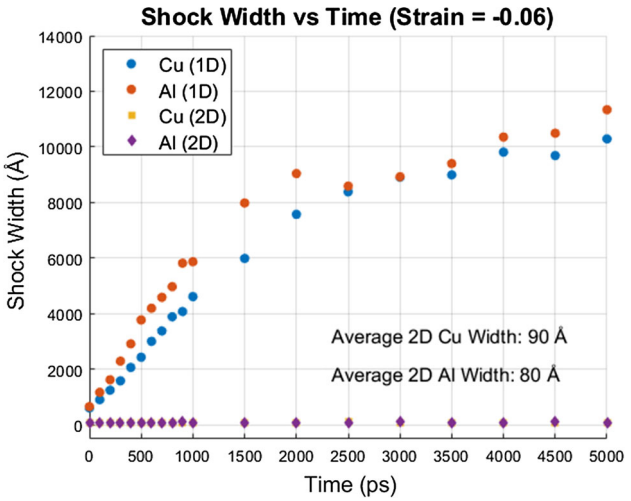

Fig. 12 Spatial shock width over time. The blue and red circles represent the 1D CAC data from [58] for both Cu and Al respectively. The gold squares and purple diamonds represent the 2D CAC data for Cu and Al from the present work

to the direction of shock propagation plays a large role in the overall steadiness of the wave. These results are similar to findings from previous NEMD studies which observed a change in shock structure and steadiness when transitioning from a 1D to 3D regime [6]. In particular, the transition from unsteady to steady waves was due to the "increase in coupling between vibrational excitations normal and transverse to the direction of shock wave propagation" [92]. Our work shows this for two dimensions as well.

7.3 Framework speedup and efficiency

For the sake of completeness, we now present results for speedup/efficiency tests which compare the two-dimensional moving window CAC framework to equally-sized NEMD domains. The data from these two studies can be seen in Fig. 13. Specifically, in Fig. 13a, we maintain a constant ratio in the CAC lattice such that the fine-scaled region is always one-tenth the length of the entire grid, and we run simulations for increasing domain sizes. We observe the CAC vs. MD speedup reach an asymptotic value around 4.0x (further increases in domain size did not significantly effect the speedup). Next, in Fig. 13b, we keep the total lattice size constant and vary the length of the coarse-scaled region from 0% to 100% of the total area. Clearly, as the percentage of the lattice that is coarse-scaled increases, the speedup does as well up to a maximum value of approximately 6.5x. These studies demonstrate the utility of using the present CAC framework to enhance performance in large-scale simulations.

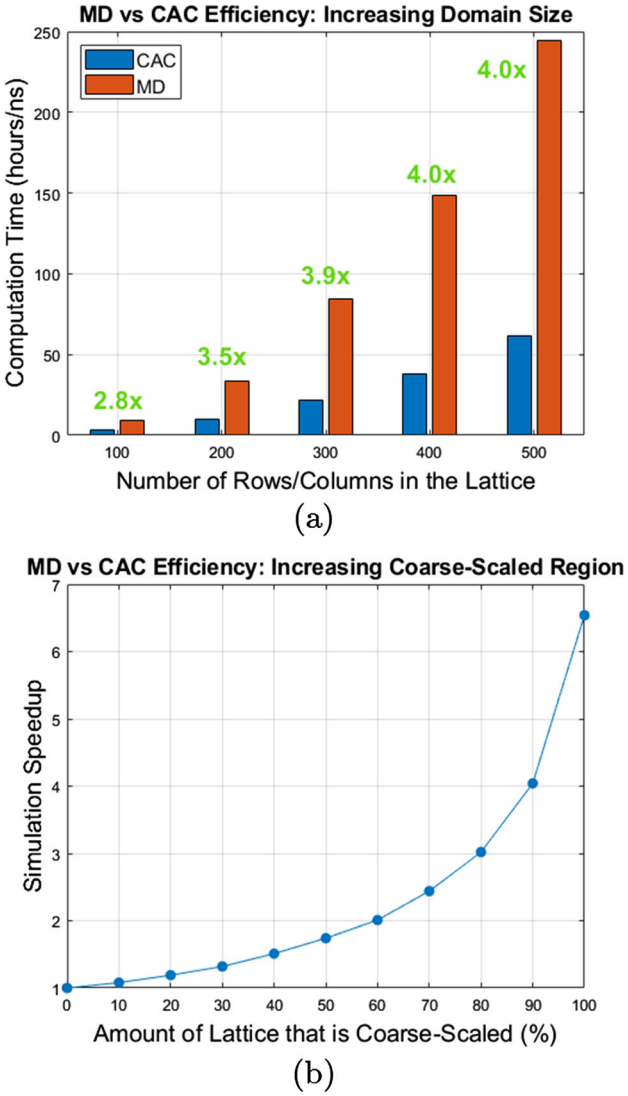

Fig. 13 Efficiency of the CAC framework vs equally-sized MD domains. In **a**, the total runtimes are compared for increasing system sizes. Here, the central fine-scaled region of the CAC lattice is always 1/10 the length of the entire grid. In **b**, the simulation speedup is shown when the size of the domain remains constant, but the coarse-scaled region increases from 0 to 100% of the lattice

8 Conclusion

In this paper, we developed a dynamic moving window CAC framework to simulate shock wave propagation through a two-dimensional, single-crystal lattice. Specifically, we characterized the shock using both the linear Hugoniot [2] and nonlinear Eulerian [59] shock equations to analyze the well-known Riemann problem of a single discontinuity traveling through an infinite medium. The CAC multiscale formulation was utilized for its ability to seamlessly transition between the fine-scaled and coarse-scaled regions, and many verifications and analyses were conducted on the higher-dimensional system. We elaborated on the technique to initialize the shock

front in the lattice as well as described two moving window methods which were incorporated into the domain. These schemes provided a mechanism to study the evolution of the shock over very long simulation times by preventing non-physical wave reflections at the A–C interfaces.

We performed many shock wave simulations within the CAC framework and used the moving window techniques to track the shock front through two different FCC materials: Cu and Al. The unique lattice directions inherent to the CAC formulation provided us the opportunity to study how directional anisotropies in single crystals can give rise to orientation-dependent shock velocities. We observed that longitudinal shocks traveling along the [112] and $[\bar{1}10]$ directions of the CAC domain propagated at distinct velocities for a given strain and particle velocity. These shock velocities were also different from those predicted by polycrystalline Hugoniot and Eulerian analytical models as well as previous one-dimensional atomistic and multiscale data. From these results, we were able to derive new Hugoniot parameters for the CAC formulation, and longitudinal stress calculations further validated the observed anisotropic material response. Our data agreed qualitatively with the results from previous NEMD studies which identified this orientation-dependence of shock evolution in solids [86–89].

Next, in Sect. 7, we exhibited the capability and novelty of the present framework by using the coarsen-refine technique to track a propagating shock wave through the entire grid. By leveraging concepts from previous atomistic and finite element schemes as well as exploiting the unique qualities of the CAC formulation, the fine-scaled region could travel through the domain at the speed of the moving wave front, and we noted the significance of this for advancing non-equilibrium multiscale research. We utilized this techinique to study the shock's structure and planarity over very long runtimes which are typically unattainable in traditional NEMD methods. Finally, we presented multiple plots comparing the efficiency of an NEMD system to an equally-sized CAC lattice. We observed that the present moving window multiscale scheme had significantly faster runtimes for various domain sizes—a necessary quality for realistic and scalable atomistic–continuum models.

The present work is innovative in its own right, but it also opens the door to more complex research involving the use of multiscale domains to simulate dynamic, nonlinear phenomena over engineering length scales. While we focused only on elastic shock waves in this work, we hope to expand this formulation to model elastic-plastic shocks [65] in polycrystalline materials to study the role of grain boundaries on shock evolution. Additionally, recent works have used both atomistic [93,94] as well as multiscale [55,95,96] methods to predict material behavior in composites and high-entropy alloys. This work provides a framework to study shock propagation through such materials. Furthermore, we would also like to utilize machine learning algorithms in this scheme to pass information from the mesoscale to macroscale [97]. Finally, we hope to incorporate a high-frequency wave passing technique that was first introduced in [49,54] into the present formulation to study shock scattering and the role of scattered waves in subsequent material behavior.

Acknowledgements This material is based upon work supported by the National Science Foundation under Grant No. 1950488. Financial support was also provided by the U.S. Department of Defense through the National Defense Science and Engineering Graduate (NDSEG) Fellowship Program (F-1656215698). Simulations were performed using the Easley computing cluster at Auburn University.

Data availability Data will be made available upon request.

Declarations

Conflict of interest The authors declare that they have no known competing financial interests or personal relationships that could have appeared to influence the work reported in this paper

Appendix A: Verifications

In this section, we present results from additional studies which verify that the current CAC framework functions correctly.

A.1 Temperature equilibration

First, we verify that the two-dimensional CAC framework used in the shock wave simulations (Fig. 4) can attain the proper canonical ensemble in the undamped WR when the Langevin thermostat is assigned to each TR. In particular, we demonstrate that the system equilibrates to the proper steady-state value over long simulation times for a range of input temperatures. The initial random velocities of the particles are such that the system has the correct total energy for a given temperature θ_0. Furthermore, we ensure that each atomistic TR has a length which is at least equal to the force range of the interatomic potential, and we set the damping parameter ζ equal to one-half the Debye frequency of the material ($\frac{1}{2}\omega_D$). These specifications are based off results from previous multiscale studies which used CADD [79] as well as CAC [58] to characterize the domain. The temperature equilibration results for both Cu and Al can be seen in Fig. 14.

The domain size for these simulations is as follows: 200 total columns (100 in the atomistic region and 50 in each continuum region) and 40 total rows. Within the fine-scaled region, there are 5 columns in each TR and hence 90 columns in the undamped WR. Each simulation is performed for 1 ns, and we use the equipartition theorem to calculate the temperature in the WR at every time step. As stated in Sect. 3.3,

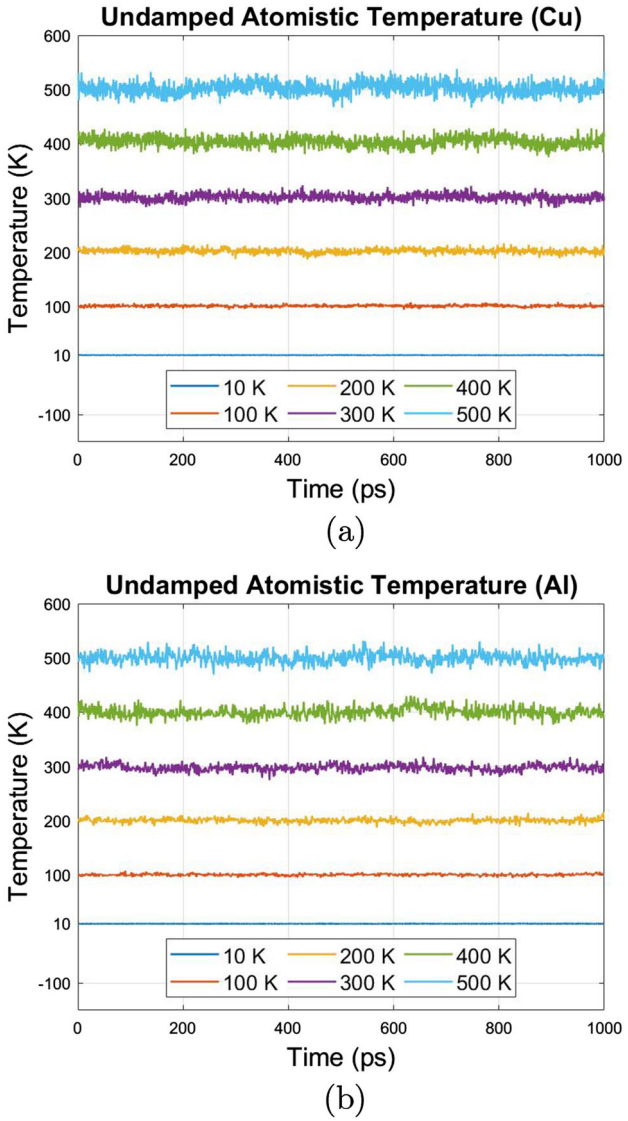

Fig. 14 Temperature in the undamped atomistic region of the CAC framework vs. time using the *Morse* potential for both **a** Cu and **b** Al. We apply the *Langevin* thermostat to the TRs with the following input temperatures: 10 K, 100 K, 200 K, 300 K, 400 K, and 500 K

the maximum temperature obtained from shock loading in this work is ~ 450 K, so we perform analysis for the following temperatures: 10 K, 100 K, 200 K, 300 K, 400 K, and 500 K. In Fig. 14, we observe that in each simulation, the temperature achieves a steady state around its mean value with very little deviation. Hence, this confirms the implementation of the framework from Fig. 4 and shows that the WR can maintain the correct equilibrium temperature during long runtimes with both materials.

A.2 Stress–strain relations

Next, we identify the elastic zone of the framework and ensure that the yield strength between a purely atomistic domain and equally-sized CAC domain is comparable. This is done to establish that the CAC force calculations are accurate as well as provide a range of input strains for the shock equations. Specifically, we compress the grid uniaxially along the x-direction ([112] lattice orientation) with strains ranging from 0.01 to 0.2 and calculate the virial stress of the domain for each input strain using the following expression [35]:

$$\sigma_{kl} = \frac{1}{A}\Bigg\langle -\sum_{\alpha} m^{\alpha}\left(\dot{u}_k^{\alpha} - \bar{\dot{u}}_k\right)\left(\dot{u}_l^{\alpha} - \bar{\dot{u}}_l\right) + \frac{1}{2}\sum_{\substack{\alpha,\beta \\ (\alpha\neq\beta)}} \varphi^{\alpha\beta}\frac{r_k^{\alpha\beta} r_l^{\alpha\beta}}{r^{\alpha\beta}}\Bigg\rangle. \tag{A1}$$

In Eq. (A1), $\boldsymbol{\sigma}$ is the virial (thermodynamic) stress, A is the area of the grid, m^{α} is the mass of particle α, $\dot{u}_k^{\alpha}$ is the velocity in the kth direction of particle α, $\bar{\dot{u}}_k$ is the average velocity in the kth direction of all particles in the given area, $\varphi^{\alpha\beta}$ is the first derivative of the potential energy at a distance $r^{\alpha\beta}$ between particles α and β ($\varphi^{\alpha\beta} = \frac{\partial \Pi}{\partial r^{\alpha\beta}}$), and $r_k^{\alpha\beta}$ is the distance in the kth direction between particles α and β. Since we consider uniaxial compressive strains for the shock simulations, we only calculate the longitudinal stress ($\sigma_{kk} = \sigma_{xx}$) in this section and do not perform any tensile tests. The stress vs. strain results for both Cu and Al at 450 K can be seen in Fig. 15.

For each atomistic simulation, the domain contains 100 columns and 20 rows, and the runtime is 100 ps with an equilibration time of 50 ps. The parameters for the CAC simulations are the same, but the lattice described in Sect. 3.1 (with damped atoms) is utilized instead of the fully atomistic grid. Since 450 K is the highest temperature achieved in the shock simulations, we specifically wanted to identify the yield point at this extreme temperature to inform our shock calculations. In Fig. 15, we observe that the linear elastic region of the CAC framework is nearly identical to that of the atomistic framework for both Cu and Al with yielding occurring at compressive strains of approximately 10% and 9% respectively. After this point, dislocations begin appearing throughout the lattice in both the coarse-scaled and fine-scaled regions, so we maintain compressive strains $\leq 9\%$ for Cu and $\leq 8\%$ for Al when using the Hugoniot and Eulerian shock equations. We note that experimental HEL values for Cu and Al are on the order of 10s to 100s of MPa largely due to pre-existing defects present in bulk metals. Since homogeneously nucleating a dislocation in a perfect crystal is much harder than moving a dislocation which already exists in the microstructure, it makes sense that the HEL values observed in the present work are higher than those obtained experimentally.

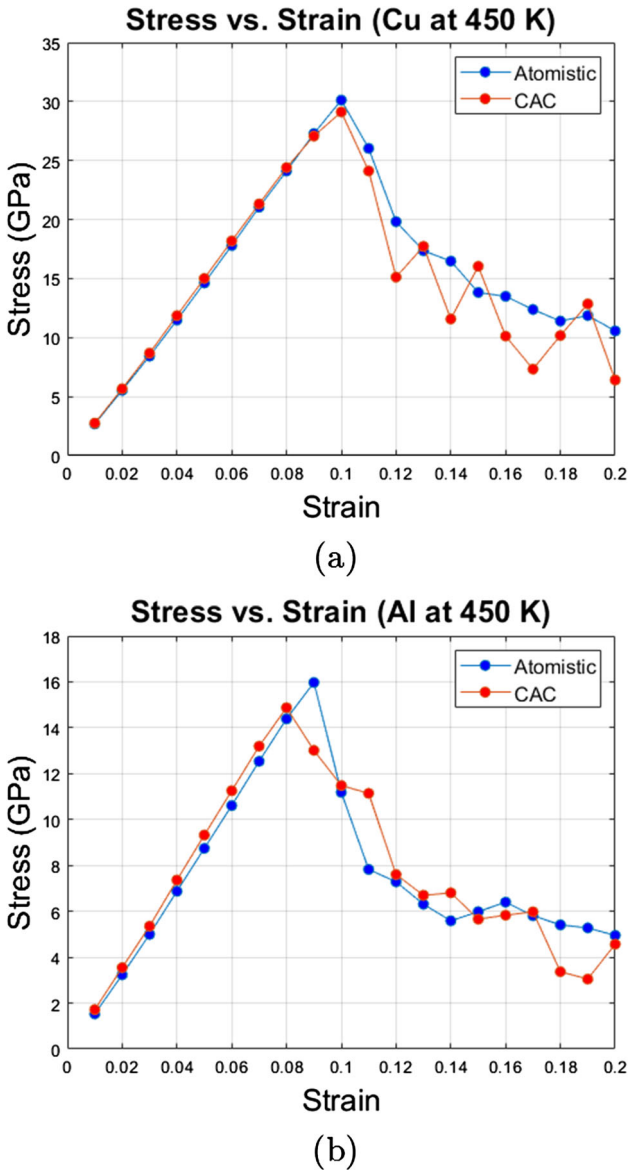

Fig. 15 Virial stress of the domain as a function of strain for both **a** Cu and **b** Al. Simulations were performed for both a purely atomistic (blue) and CAC (red) framework. In each case, the system is equilibrated to 450 K, and the compression is applied uniaxially along the x-direction

These results confirm the validity of the CAC force calculations, and they are also congruent with results from previous CAC studies [42,98,99].

Appendix B: Additional information on 2D CAC elements

B.1 Mass matrix

We now elaborate on the isoparametric formulation of the mass matrix for a given continuum element in the 2D CAC framework. As stated in Sect. 4.2, element connectivity is not required in CAC. Hence, this derivation is general and can be applied to any element in the domain assuming the physical nodal coordinates of that element are known.

The isoparametric shape functions of a four-node element are given as follows:

$$\phi_1(\xi,\eta) = \frac{1}{4}(1-\xi)(1-\eta) \tag{B2}$$

$$\phi_2(\xi,\eta) = \frac{1}{4}(1+\xi)(1-\eta) \tag{B3}$$

$$\phi_3(\xi,\eta) = \frac{1}{4}(1-\xi)(1+\eta) \tag{B4}$$

$$\phi_4(\xi,\eta) = \frac{1}{4}(1+\xi)(1+\eta) \tag{B5}$$

which can be stored in a matrix as

$$\boldsymbol{\Phi}(\xi,\eta) = \begin{bmatrix} \phi_1 & 0 & \phi_2 & 0 & \phi_3 & 0 & \phi_4 & 0 \\ 0 & \phi_1 & 0 & \phi_2 & 0 & \phi_3 & 0 & \phi_4 \end{bmatrix} \tag{B6}$$

where $\phi_i = \phi_i(\xi,\eta)$. In order to map the element between the global and natural coordinate system, we need the Jacobian which is given as follows:

$$\boldsymbol{J} = \begin{bmatrix} \partial\phi_1/\partial\xi & \partial\phi_2/\partial\xi & \partial\phi_3/\partial\xi & \partial\phi_4/\partial\xi \\ \partial\phi_1/\partial\eta & \partial\phi_2/\partial\eta & \partial\phi_3/\partial\eta & \partial\phi_4/\partial\eta \end{bmatrix} \begin{bmatrix} x_1 & y_1 \\ x_2 & y_2 \\ x_3 & y_3 \\ x_4 & y_4 \end{bmatrix} \tag{B7}$$

where (x_1, y_1), (x_2, y_2), (x_3, y_3), and (x_4, y_4) are the positions of the four element nodes in the global coordinate system. We note that the numbering goes counterclockwise starting from the left node as seen in Fig. 16.

Expanding out Eq. (B7) and taking the appropriate derivatives of the shape functions, we obtain the four components of the Jacobian:

$$J_1 = \frac{x_1}{4}(\eta-1) + \frac{x_2}{4}(1-\eta) + \frac{x_3}{4}(\eta+1) - \frac{x_4}{4}(\eta+1) \tag{B8}$$

$$J_2 = \frac{y_1}{4}(\eta-1) + \frac{y_2}{4}(1-\eta) + \frac{y_3}{4}(\eta+1) - \frac{y_4}{4}(\eta+1) \tag{B9}$$

$$J_3 = \frac{x_1}{4}(\xi-1) - \frac{x_2}{4}(\xi+1) + \frac{x_3}{4}(\xi+1) + \frac{x_4}{4}(1-\xi) \tag{B10}$$

$$J_4 = \frac{y_1}{4}(\xi-1) - \frac{y_2}{4}(\xi+1) + \frac{y_3}{4}(\xi+1) + \frac{y_4}{4}(1-\xi). \tag{B11}$$

Hence, the Jacobian determinant is

$$det(\mathbf{J}) = \begin{vmatrix} J_1 & J_2 \\ J_3 & J_4 \end{vmatrix} = J_1 J_4 - J_2 J_3 \tag{B12}$$

which can be simplified using a software program like Wolfram Mathematica.

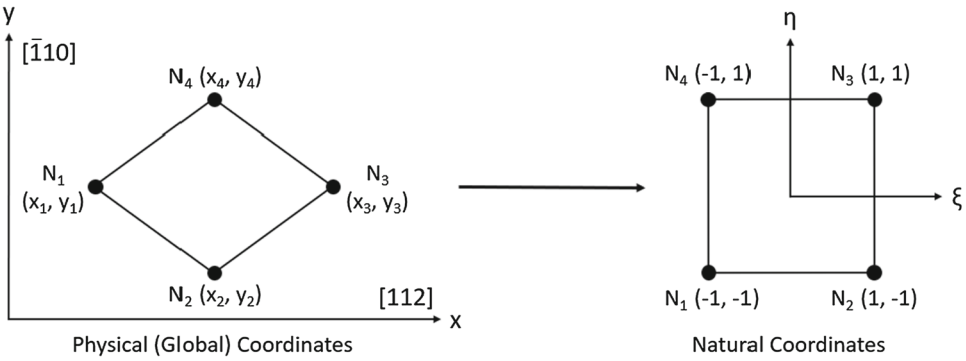

Fig. 16 Mapping from global to natural coordinates of a two-dimensional CAC element

The expression for the mass matrix of the 2D element in global coordinates is given as follows:

$$\mathbf{M} = \rho \int_A \mathbf{\Phi}^T \mathbf{\Phi} \, dA. \tag{B13}$$

Writing this in natural coordinates:

$$\mathbf{M} = \rho \int_{-1}^{1} \int_{-1}^{1} \left[\mathbf{\Phi}^T \mathbf{\Phi} \cdot det(\mathbf{J}) \right] d\xi d\eta \tag{B14}$$

where

$$\mathbf{\Phi}^T \mathbf{\Phi} = \begin{bmatrix} \phi_1 & 0 \\ 0 & \phi_1 \\ \phi_2 & 0 \\ 0 & \phi_2 \\ \phi_3 & 0 \\ 0 & \phi_3 \\ \phi_4 & 0 \\ 0 & \phi_4 \end{bmatrix} \begin{bmatrix} \phi_1 & 0 & \phi_2 & 0 & \phi_3 & 0 & \phi_4 & 0 \\ 0 & \phi_1 & 0 & \phi_2 & 0 & \phi_3 & 0 & \phi_4 \end{bmatrix} \tag{B15}$$

and ρ is the area of the element. As a result, we can use the expressions for the shape functions as well as $det(\mathbf{J})$ from Eq. (B12) to calculate all sixty-four components of the mass matrix for the given element. It turns out, however, that only ten of these components are unique, so we can simplify the mass matrix significantly as follows:

$$\mathbf{M} = \begin{bmatrix} M_{11} & M_{13} & M_{15} & M_{17} \\ M_{13} & M_{33} & M_{35} & M_{37} \\ M_{15} & M_{35} & M_{55} & M_{57} \\ M_{17} & M_{37} & M_{57} & M_{77} \end{bmatrix} \tag{B16}$$

where

$$M_{ij} = \rho \int_{-1}^{1} \int_{-1}^{1} \left[\phi_i \phi_j \cdot det(\mathbf{J}) \right] d\xi d\eta. \tag{B17}$$

After obtaining the cumulative force on each node in the element through Gaussian integration (see Appendix B.2), we can then calculate the respective accelerations as follows:

$$\begin{bmatrix} \ddot{\mathbf{u}}_1 \\ \ddot{\mathbf{u}}_2 \\ \ddot{\mathbf{u}}_3 \\ \ddot{\mathbf{u}}_4 \end{bmatrix} = \begin{bmatrix} M_{11} & M_{13} & M_{15} & M_{17} \\ M_{13} & M_{33} & M_{35} & M_{37} \\ M_{15} & M_{35} & M_{55} & M_{57} \\ M_{17} & M_{37} & M_{57} & M_{77} \end{bmatrix}^{-1} \begin{bmatrix} \mathbf{f}_1 \\ \mathbf{f}_2 \\ \mathbf{f}_3 \\ \mathbf{f}_4 \end{bmatrix}. \tag{B18}$$

In this work, we use the lumped mass matrix approximation, and specifically, the row-sum method. Hence, we can further simplify our calculations and sum the rows of the mass matrix such that

$$M_1 = M_{11} + M_{13} + M_{15} + M_{17} \tag{B19}$$
$$M_2 = M_{13} + M_{33} + M_{35} + M_{37} \tag{B20}$$
$$M_3 = M_{15} + M_{35} + M_{55} + M_{57} \tag{B21}$$
$$M_4 = M_{17} + M_{37} + M_{57} + M_{77}. \tag{B22}$$

Therefore, we arrive at the final result for the accelerations of the four nodes:

$$\begin{bmatrix} \ddot{\mathbf{u}}_1 \\ \ddot{\mathbf{u}}_2 \\ \ddot{\mathbf{u}}_3 \\ \ddot{\mathbf{u}}_4 \end{bmatrix} = \begin{bmatrix} \mathbf{f}_1/M_1 \\ \mathbf{f}_2/M_2 \\ \mathbf{f}_3/M_3 \\ \mathbf{f}_4/M_4 \end{bmatrix}. \tag{B23}$$

For the sake of completeness, we provide the expressions for the ten unique components of the two-dimensional mass matrix below. As can be seen, each of these terms is strictly a function of the four nodal positions of the element in the global coordinate system as well as the density ρ. Thus, assuming that we know the global coordinates, we can calculate each component of the mass matrix and thereby obtain

the acceleration of each node.

$$M_{11} = \frac{\rho}{36}[(3x_1 - x_3)(y_2 - y_4) + x_2(2y_4 + y_3 - 3y_1) + x_4(3y_1 - 2y_2 - y_3)] \quad \text{(B24)}$$

$$M_{13} = \frac{\rho}{72}[x_1(3y_2 - y_3 - 2y_4) + x_2(y_4 + 2y_3 - 3y_1) + x_3(y_1 - 2y_2 + y_4) + x_4(2y_1 - y_2 - y_3)] \quad \text{(B25)}$$

$$M_{15} = \frac{\rho}{72}[(x_1 - x_3)(y_2 - y_4) - (x_2 - x_4)(y_1 - y_3)] \quad \text{(B26)}$$

$$M_{17} = \frac{\rho}{72}[x_1(2y_2 + y_3 - 3y_4) + x_2(y_4 + y_3 - 2y_1) - x_3(y_1 + y_2 - 2y_4) + x_4(3y_1 - y_2 - 2y_3)] \quad \text{(B27)}$$

$$M_{33} = \frac{\rho}{36}[x_1(3y_2 - 2y_3 - y_4) + 3x_2(y_3 - y_1) + x_3(2y_1 - 3y_2 + y_4) + x_4(y_1 - y_3)] \quad \text{(B28)}$$

$$M_{35} = \frac{\rho}{72}[x_1(2y_2 - y_3 - y_4) - x_2(2y_1 - 3y_3 + y_4) + x_3(y_1 - 3y_2 + 2y_4) + x_4(y_1 + y_2 - 2y_3)] \quad \text{(B29)}$$

$$M_{37} = \frac{\rho}{72}[(x_1 - x_3)(y_2 - y_4) - (x_2 - x_4)(y_1 - y_3)] \quad \text{(B30)}$$

$$M_{55} = \frac{\rho}{36}[(x_1 - 3x_3)(y_2 - y_4) - x_2(y_1 - 3y_3 + 2y_4) + x_4(y_1 + 2y_2 - 3y_3)] \quad \text{(B31)}$$

$$M_{57} = \frac{\rho}{72}[x_1(y_2 + y_3 - 2y_4) - x_2(y_1 - 2y_3 + y_4) - x_3(y_1 + 2y_2 - 3y_4) + x_4(2y_1 + y_2 - 3y_3)] \quad \text{(B32)}$$

$$M_{77} = \frac{\rho}{36}[x_1(y_2 + 2y_3 - 3y_4) + x_2(y_3 - y_1) - x_3(2y_1 + y_2 - 3y_4) + 3x_4(y_1 - y_3)] \quad \text{(B33)}$$

B.2 Gaussian integration

For this work, we calculate the internal force density using Gaussian integration, so we now elaborate on this method for a 2D coarse-scaled element. In Gaussian integration, the elemental forces are approximated by the forces at both the nodes as well as the integration points. Thus, while more complex to implement, Gaussian integration typically results in more accurate force calculations when using complex geometries or large elements. For all of our simulations, we use twelve-point Gaussian integration such that each element, in addition to the four nodes, contains twelve integration points. These integration points are chosen such that there are two along each edge of the element and four on the interior surface as seen in Fig. 17. In particular, both the edge and surface integration points are chosen to be equal to the lattice points which directly neighbor the nodes, and this is comparable to techniques used in other multiscale schemes such as cluster-QC [100] and three-dimensional CAC [67].

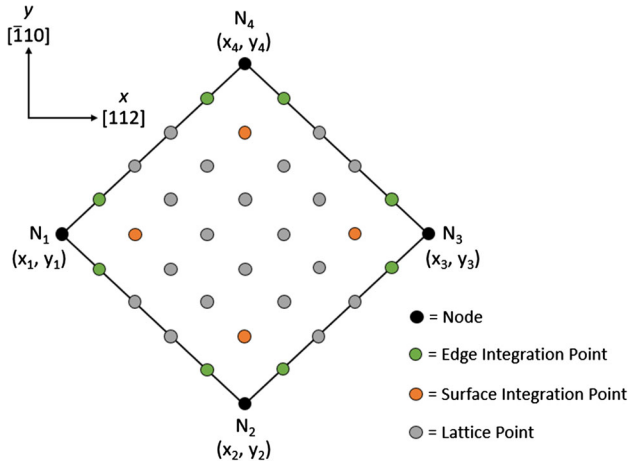

Fig. 17 Two-dimensional CAC coarse-scaled element. Nodes are shown in black, edge integration points are shown in green, surface integration points are shown in orange, and lattice points are shown in grey

The forces within the 2D element are thus split into three distinct parts associated with the (1) nodes, (2) edges, and (3) surfaces as seen in the equation below:

$$\mathbf{F}_{int} = \mathbf{FN}_{int} + \mathbf{FE}_{int} + \mathbf{FS}_{int}. \quad \text{(B34)}$$

The first term in Eq. (B34) represents the forces at the nodes and is given by Eq. (B37), where we note that all of the weights equal one. Additionally, each shape function equals one at its nodal location and zero everywhere else. Equation (B37) would be the only force used in nodal integration—a technique which effectively does not alter the forces obtained using the interatomic potential function and relative displacement of particles. Although nodal integration is more computationally efficient, it is less robust than Gaussian integration and only accurate for simple geometries and relatively small elements, so it is not used in this work.

The second two forces in Eq. (B34) are given as follows:

$$\mathbf{FE}_{int} = \sum_{j=1}^{8}(w_{j,x} \cdot w_{j,y})\mathbf{\Phi}(j)\mathbf{f}_{int}(j) \quad \text{(B35)}$$

$$\mathbf{FS}_{int} = \sum_{j=9}^{12}(w_{j,x} \cdot w_{j,y})\mathbf{\Phi}(j)\mathbf{f}_{int}(j). \quad \text{(B36)}$$

In Eqs. (B35) and (B36), the summations occur over the eight edge integration points and four surface integration points

respectively. Furthermore, the terms $w_{j,x}$ and $w_{j,y}$ are the weights of the integration points along the x and y directions. Finally, $\mathbf{\Phi}(j)$ is the shape function vector at the given integration point while $\mathbf{f}_{int}(j)$ is the force of the integration point obtained through the potential function. For the sake simplicity, we do not write out the full expressions of these terms, but the expansion would be similar to that shown for the nodal forces in Eq. (B37).

$$\begin{aligned}
\mathbf{FN}_{int} &= w_{N_1}\mathbf{\Phi}(N_1)\mathbf{f}_{int}(N_1) + w_{N_2}\mathbf{\Phi}(N_2)\mathbf{f}_{int}(N_2) \\
&\quad + w_{N_3}\mathbf{\Phi}(N_3)\mathbf{f}_{int}(N_3) + w_{N_4}\mathbf{\Phi}(N_4)\mathbf{f}_{int}(N_4) \\
&= \begin{bmatrix} \phi_1(N_1) \\ \phi_2(N_1) \\ \phi_3(N_1) \\ \phi_4(N_1) \end{bmatrix} \mathbf{f}_{int}(N_1) + \begin{bmatrix} \phi_1(N_2) \\ \phi_2(N_2) \\ \phi_3(N_2) \\ \phi_4(N_2) \end{bmatrix} \mathbf{f}_{int}(N_2) \\
&\quad + \begin{bmatrix} \phi_1(N_3) \\ \phi_2(N_3) \\ \phi_3(N_3) \\ \phi_4(N_3) \end{bmatrix} \mathbf{f}_{int}(N_3) + \begin{bmatrix} \phi_1(N_4) \\ \phi_2(N_4) \\ \phi_3(N_4) \\ \phi_4(N_4) \end{bmatrix} \mathbf{f}_{int}(N_4) \\
&= \begin{bmatrix} 1 \\ 0 \\ 0 \\ 0 \end{bmatrix} \mathbf{f}_{int}(x_1, y_1) + \begin{bmatrix} 0 \\ 1 \\ 0 \\ 0 \end{bmatrix} \mathbf{f}_{int}(x_2, y_2) \\
&\quad + \begin{bmatrix} 0 \\ 0 \\ 1 \\ 0 \end{bmatrix} \mathbf{f}_{int}(x_3, y_3) + \begin{bmatrix} 0 \\ 0 \\ 0 \\ 1 \end{bmatrix} \mathbf{f}_{int}(x_4, y_4) \\
&= \left[\mathbf{f}_{int}(x_1, y_1)\ \mathbf{f}_{int}(x_2, y_2)\ \mathbf{f}_{int}(x_3, y_3)\ \mathbf{f}_{int}(x_4, y_4)\right]^T
\end{aligned} \tag{B37}$$

References

1. Meyers MA (1994) Dynamic behavior of materials. Wiley, Hoboken
2. Davison L (2008) Fundamentals of shock wave propagation in solids. Springer, Berlin
3. Gray GT III (2012) High-strain-rate deformation: mechanical behavior and deformation substructures induced. Annu Rev Mater Res 42:285–303. https://doi.org/10.1146/annurev-matsci-070511-155034
4. Fensin S, Escobedo J, Gray G III et al (2014) Dynamic damage nucleation and evolution in multiphase materials. J Appl Phys. https://doi.org/10.1063/1.4880435
5. Bingert JF, Suter RM, Lind J et al (2014) High-energy diffraction microscopy characterization of spall damage. In: Dynamic behavior of materials, volume 1. Springer, pp 397–403. https://doi.org/10.1007/978-3-319-00771-7_48
6. Holian B (1995) Atomistic computer simulations of shock waves. Shock Waves 5(3):149–157. https://doi.org/10.1007/BF01435522
7. Germann TC, Holian BL, Lomdahl PS et al (2004) Dislocation structure behind a shock front in fcc perfect crystals: atomistic simulation results. Metall Mater Trans A 35(9):2609–2615. https://doi.org/10.1007/s11661-004-0206-5
8. Tramontina D, Hahn E, Meyers M, et al (2017) Simulation of tantalum nanocrystals under shock-wave loading: dislocations and twinning. In: AIP conference proceedings. AIP Publishing LLC. https://doi.org/10.1063/1.4971590
9. Righi G, Ruestes CJ, Stan CV et al (2021) Towards the ultimate strength of iron: spalling through laser shock. Acta Materialia. https://doi.org/10.1016/j.actamat.2021.117072
10. Zhu Q, Shao JL, Pan H et al (2021) Collapse of stacking fault tetrahedron and dislocation evolution in copper under shock compression. J Nucl Mater. https://doi.org/10.1016/j.jnucmat.2021.153081
11. Higginbotham A, Suggit M, Bringa EM et al (2013) Molecular dynamics simulations of shock-induced deformation twinning of a body-centered-cubic metal. Phys Rev B. https://doi.org/10.1103/PhysRevB.88.104105
12. Wu D, Chen K, Zhu Y et al (2021) Unveiling grain size effect on shock-induced plasticity and its underlying mechanisms in nano-polycrystalline Ta. Mech Mater. https://doi.org/10.1016/j.mechmat.2021.103952
13. Zhu Y, Wu D, Zhao L et al (2021) A novel shock-induced multistage phase transformation and underlying mechanism in textured nano-twinned Cu. Extreme Mech Lett. https://doi.org/10.1016/j.eml.2021.101448
14. Bringa EM, Traiviratana S, Meyers MA (2010) Void initiation in fcc metals: effect of loading orientation and nanocrystalline effects. Acta Materialia 58(13):4458–4477. https://doi.org/10.1016/j.actamat.2010.04.043
15. Bisht A, Neogi A, Mitra N et al (2019) Investigation of the elastically shock-compressed region and elastic–plastic shock transition in single-crystalline copper to understand the dislocation nucleation mechanism under shock compression. Shock Waves 29(7):913–927. https://doi.org/10.1007/s00193-018-00887-8
16. Tian X, Ma K, Ji G et al (2021) Anisotropic shock responses of nanoporous al by molecular dynamics simulations. PLoS ONE. https://doi.org/10.1371/journal.pone.0247172
17. Srinivasan S, Baskes M, Wagner G (2007) Atomistic simulations of shock induced microstructural evolution and spallation in single crystal nickel. J Appl Phys. https://doi.org/10.1063/1.2423084
18. Fensin S, Escobedo-Diaz J, Brandl C et al (2014) Effect of loading direction on grain boundary failure under shock loading. Acta Materialia 64:113–122. https://doi.org/10.1016/j.actamat.2013.11.026
19. Wang XX, He AM, Zhou TT et al (2021) Spall damage in single crystal tin under shock wave loading: a molecular dynamics simulation. Mech Mater. https://doi.org/10.1016/j.mechmat.2021.103991
20. Chen Y, Jian Z, Xiao S et al (2021) Molecular dynamics simulation of shock wave propagation and spall failure in single crystal copper under cylindrical impact. Appl Phys Express. https://doi.org/10.35848/1882-0786/ac06de
21. Dewapriya M, Miller R (2021) Molecular dynamics simulations of shock propagation and spallation in amorphous polymers. J Appl Mech. https://doi.org/10.1115/1.4051238
22. Diehl P, Lipton R, Wick T et al (2022) A comparative review of peridynamics and phase-field models for engineering fracture mechanics. Comput Mech 69:1259–1293. https://doi.org/10.1007/s00466-022-02147-0
23. Reed EJ, Fried LE, Joannopoulos J (2003) A method for tractable dynamical studies of single and double shock compression. Phys Rev Lett. https://doi.org/10.1103/PhysRevLett.90.235503
24. Reed EJ, Fried LE, Henshaw WD et al (2006) Analysis of simulation technique for steady shock waves in materials with analytical equations of state. Phys Rev E. https://doi.org/10.1103/PhysRevE.74.056706

25. Maillet JB, Mareschal M, Soulard L et al (2000) Uniaxial hugoniostat: a method for atomistic simulations of shocked materials. Phys Rev E. https://doi.org/10.1103/PhysRevE.63.016121
26. Maillet JB, Bernard S (2002) Uniaxial hugoniostat: method and applications. In: AIP conference proceedings. American Institute of Physics, pp 367–370. https://doi.org/10.1063/1.1483555
27. Zhakhovskii V, Nishihara K, Anisimov S (1997) Shock wave structure in dense gases. J Exp Theor Phys Lett 66(2):99–105. https://doi.org/10.1134/1.567510
28. Zhakhovsky VV, Budzevich MM, Inogamov NA et al (2011) Two-zone elastic–plastic single shock waves in solids. Phys Rev Lett. https://doi.org/10.1103/PhysRevLett.107.135502
29. Davis A, Agrawal V (2020) One-dimensional moving window atomistic framework to model long-time shock wave propagation. Comput Methods Appl Mech Eng. https://doi.org/10.1016/j.cma.2020.113290
30. Kohlhoff S, Gumbsch P, Fischmeister H (1991) Crack propagation in bcc crystals studied with a combined finite-element and atomistic model. Philos Mag A 64(4):851–878. https://doi.org/10.1080/01418619108213953
31. McDowell DL (2020) Connecting lower and higher scales in crystal plasticity modeling. Handbook of materials modeling: methods: theory and modeling, pp 1609–1629. https://doi.org/10.1007/978-3-319-44677-6_17
32. Van Der Giessen E, Schultz PA, Bertin N et al (2020) Roadmap on multiscale materials modeling. Model Simul Mater Sci Eng. https://doi.org/10.1088/1361-651X/ab7150
33. Xiong L, Chen Y, Beyerlein IJ et al (2021) Multiscale modeling of interface-mediated mechanical, thermal, and mass transport in heterogeneous materials: perspectives and applications. J Mater Res 36(13):2601–2614. https://doi.org/10.1557/s43578-021-00293-4
34. Fish J, Wagner GJ, Keten S (2021) Mesoscopic and multiscale modelling in materials. Nat Mater 20(6):774–786. https://doi.org/10.1038/s41563-020-00913-0
35. Tadmor EB, Miller RE (2011) Modeling materials: continuum, atomistic and multiscale techniques. Cambridge University Press, Cambridge
36. Shilkrot L, Miller RE, Curtin W (2002) Coupled atomistic and discrete dislocation plasticity. Phys Rev Lett. https://doi.org/10.1103/PhysRevLett.89.025501
37. Xiao S, Belytschko T (2004) A bridging domain method for coupling continua with molecular dynamics. Comput Methods Appl Mech Eng 193(17–20):1645–1669. https://doi.org/10.1016/j.cma.2003.12.053
38. Rudd RE, Broughton JQ (1998) Coarse-grained molecular dynamics and the atomic limit of finite elements. Phys Rev B 58(10):893–896. https://doi.org/10.1103/PhysRevB.58.R5893
39. Tadmor EB, Ortiz M, Phillips R (1996) Quasicontinuum analysis of defects in solids. Philos Mag A 73(6):1529–1563. https://doi.org/10.1080/01418619608243000
40. Chen Y, Lee J (2005) Atomistic formulation of a multiscale field theory for nano/micro solids. Philos Mag 85(33–35):4095–4126. https://doi.org/10.1080/14786430500362595
41. Chen Y (2009) Reformulation of microscopic balance equations for multiscale materials modeling. J Chem Phys. https://doi.org/10.1063/1.3103887
42. Xiong L, Tucker G, McDowell DL et al (2011) Coarse-grained atomistic simulation of dislocations. J Mech Phys Solids 59(2):160–177. https://doi.org/10.1016/j.jmps.2010.11.005
43. Zeng X, Wang X, Lee JD et al (2011) Multiscale modeling of nano/micro systems by a multiscale continuum field theory. Comput Mech 47(2):205–216. https://doi.org/10.1007/s00466-010-0538-5
44. Yang S, Xiong L, Deng Q et al (2013) Concurrent atomistic and continuum simulation of strontium titanate. Acta Materialia 61(1):89–102. https://doi.org/10.1016/j.actamat.2012.09.032
45. Xiong L, Chen X, Zhang N et al (2014) Prediction of phonon properties of 1D polyatomic systems using concurrent atomistic-continuum simulation. Arch Appl Mech 84(9):1665–1675. https://doi.org/10.1007/s00419-014-0880-8
46. Xiong L, Xu S, McDowell DL et al (2015) Concurrent atomistic-continuum simulations of dislocation-void interactions in fcc crystals. Int J Plast 65:33–42. https://doi.org/10.1016/j.ijplas.2014.08.002
47. Xu S, Xiong L, Deng Q et al (2016) Mesh refinement schemes for the concurrent atomistic-continuum method. Int J Solids Struct 90:144–152. https://doi.org/10.1016/j.ijsolstr.2016.03.030
48. Chen X, Li W, Diaz A et al (2017) Recent progress in the concurrent atomistic-continuum method and its application in phonon transport. MRS Commun 7(4):785–797. https://doi.org/10.1557/mrc.2017.116
49. Chen X, Diaz A, Xiong L et al (2018) Passing waves from atomistic to continuum. J Comput Phys 354:393–402. https://doi.org/10.1016/j.jcp.2017.10.038
50. Xu S, Payne TG, Chen H et al (2018) Pycac: the concurrent atomistic-continuum simulation environment. J Mater Res 33(7):857–871. https://doi.org/10.1557/jmr.2018.8
51. Chen Y, Shabanov S, McDowell DL (2019) Concurrent atomistic-continuum modeling of crystalline materials. J Appl Phys. https://doi.org/10.1063/1.5099653
52. Xiong L, McDowell DL, Chen Y (2014) Sub-thz phonon drag on dislocations by coarse-grained atomistic simulations. Int J Plast 55:268–278. https://doi.org/10.1016/j.ijplas.2013.11.004
53. Chen X, Xiong L, McDowell DL et al (2017) Effects of phonons on mobility of dislocations and dislocation arrays. Scr Mater 137:22–26. https://doi.org/10.1016/j.scriptamat.2017.04.033
54. Davis AS, Agrawal V (2022) Transmitting multiple high-frequency phonons across length scales using the concurrent atomistic-continuum method. Comput Mater Sci. https://doi.org/10.1016/j.commatsci.2022.111702
55. Chu K, Diaz A, Chen Y et al (2022) Multiscale concurrent atomistic-continuum (cac) modeling of multicomponent alloys. Comput Mater Sci. https://doi.org/10.1016/j.commatsci.2021.110873
56. Selimov A, Xu S, Chen Y et al (2021) Lattice dislocation induced misfit dislocation evolution in semi-coherent {111} bimetal interfaces. J Mater Res 36:2763–2778. https://doi.org/10.1557/s43578-021-00184-8
57. Selimov A, Chu K, McDowell DL (2022) Coarse-grained atomistic modeling of dislocations and generalized crystal plasticity. J Micromech Mol Phys 7(2):103–125. https://doi.org/10.1142/S2424913021420133
58. Davis AS, Lloyd JT, Agrawal V (2022) Moving window techniques to model shock wave propagation using the concurrent atomistic-continuum method. Comput Methods Appl Mech Eng. https://doi.org/10.1016/j.cma.2021.114360
59. Clayton JD (2013) Nonlinear eulerian thermoelasticity for anisotropic crystals. J Mech Phys Solids 61(10):1983–2014. https://doi.org/10.1016/j.jmps.2013.05.009
60. Clayton J (2014) Shock compression of metal crystals: a comparison of Eulerian and Lagrangian elastic-plastic theories. Int J Appl Mech. https://doi.org/10.1142/S1758825114500483
61. Zimmerman JA, Winey JM, Gupta YM (2011) Elastic anisotropy of shocked aluminum single crystals: use of molecular dynamics simulations. Phys Rev B. https://doi.org/10.1103/PhysRevB.83.184113

62. Weaver JS (1976) Application of finite strain theory to non-cubic crystals. J Phys Chem Solids 37(7):711–718. https://doi.org/10.1016/0022-3697(76)90009-3
63. Perrin G, Delannoy M (1978) Application de la théorie des déformations finies à la détermination de propriétés élastiques des polycristaux de symétrie hexagonale sous haute pression. Journal de Physique 39(10):1085–1095. https://doi.org/10.1051/jphys:0197800390100108500
64. Holian B, Straub G (1978) Molecular dynamics of shock waves in one-dimensional chains. Phys Rev B 18(4):1593–1608. https://doi.org/10.1103/PhysRevB.18.1593
65. Lloyd J, Clayton J, Becker R et al (2014) Simulation of shock wave propagation in single crystal and polycrystalline aluminum. Int J Plast 60:118–144. https://doi.org/10.1016/j.ijplas.2014.04.012
66. Lloyd J, Clayton J, Austin R et al (2014) Plane wave simulation of elastic–viscoplastic single crystals. J Mech Phys Solids 69:14–32. https://doi.org/10.1016/j.jmps.2014.04.009
67. Xu S, Che R, Xiong L et al (2015) A quasistatic implementation of the concurrent atomistic-continuum method for fcc crystals. Int J Plast 72:91–126. https://doi.org/10.1016/j.ijplas.2015.05.007
68. MacDonald RA, MacDonald WM (1981) Thermodynamic properties of fcc metals at high temperatures. Phys Rev B 24(4):1715–1724. https://doi.org/10.1103/PhysRevB.24.1715
69. Schneider T, Stoll E (1978) Molecular-dynamics study of a three-dimensional one-component model for distortive phase transitions. Phys Rev B 17(3):1302–1322. https://doi.org/10.1103/PhysRevB.17.1302
70. Marsh SP (1980) LASL shock Hugoniot data. University of California press, California
71. Hiki Y, Granato A (1966) Anharmonicity in noble metals; higher order elastic constants. Phys Rev 144(2):411–419. https://doi.org/10.1103/PhysRev.144.411
72. Thomas JF Jr (1968) Third-order elastic constants of aluminum. Phys Rev 175(3):955–962. https://doi.org/10.1103/PhysRev.175.955
73. Xiong L, Chen Y (2009) Multiscale modeling and simulation of single-crystal mgo through an atomistic field theory. Int J Solids Struct 46(6):1448–1455. https://doi.org/10.1016/j.ijsolstr.2008.11.012
74. Deng Q, Xiong L, Chen Y (2010) Coarse-graining atomistic dynamics of brittle fracture by finite element method. Int J Plast 26(9):1402–1414. https://doi.org/10.1016/j.ijplas.2010.04.007
75. Chen G, Yang R, Chen X (2005) Nanoscale heat transfer and thermal-electric energy conversion. In: Journal de Physique IV (Proceedings), EDP Sciences, pp 499–504. https://doi.org/10.1051/jp4:2005125116
76. Chen Y (2006) Local stress and heat flux in atomistic systems involving three-body forces. J Chem Phys. https://doi.org/10.1063/1.2166387
77. Yang S (2014) A concurrent atomistic-continuum method for simulating defects in ionic materials. PhD thesis, University of Florida
78. Needleman A (1987) A continuum model for void nucleation by inclusion debonding. J Appl Mech 54(3):525–531. https://doi.org/10.1115/1.3173064
79. Qu S, Shastry V, Curtin W et al (2005) A finite-temperature dynamic coupled atomistic/discrete dislocation method. Model Simul Mater Sci Eng 13(7):1101–1118. https://doi.org/10.1088/0965-0393/13/7/007
80. Holland D, Marder M (1998) Ideal brittle fracture of silicon studied with molecular dynamics. Phys Rev Lett 80(4):746–749. https://doi.org/10.1103/PhysRevLett.80.746
81. Selinger RL, Corbett JM (2000) Dynamic fracture in disordered media. MRS Bull 25(5):46–50. https://doi.org/10.1557/mrs2000.73
82. Berger MJ, Colella P (1989) Local adaptive mesh refinement for shock hydrodynamics. J Comput Phys 82(1):64–84. https://doi.org/10.1016/0021-9991(89)90035-1
83. Greco F, Leonetti L, Lonetti P et al (2015) Crack propagation analysis in composite materials by using moving mesh and multiscale techniques. Comput Struct 153:201–216. https://doi.org/10.1016/j.compstruc.2015.03.002
84. Tembhekar I, Amelang JS, Munk L et al (2017) Automatic adaptivity in the fully nonlocal quasicontinuum method for coarse-grained atomistic simulations. Int J Numer Methods Eng 110(9):878–900. https://doi.org/10.1002/nme.5438
85. Amor-Martin A, Garcia-Castillo LE (2021) Adaptive semi-structured mesh refinement techniques for the finite element method. Appl Sci. https://doi.org/10.3390/app11083683
86. Germann TC, Holian BL, Lomdahl PS et al (2000) Orientation dependence in molecular dynamics simulations of shocked single crystals. Phys Rev Lett 84(23):5351–5354. https://doi.org/10.1103/PhysRevLett.84.5351
87. Bringa E, Cazamias J, Erhart P et al (2004) Atomistic shock hugoniot simulation of single-crystal copper. J Appl Phys 96(7):3793–3799. https://doi.org/10.1063/1.1789266
88. Lin E, Shi H, Niu L (2014) Effects of orientation and vacancy defects on the shock Hugoniot behavior and spallation of single-crystal copper. Model Simul Mater Sci Eng. https://doi.org/10.1088/0965-0393/22/3/035012
89. Neogi A, Mitra N (2017) Shock induced deformation response of single crystal copper: effect of crystallographic orientation. Comput Mater Sci 135:141–151. https://doi.org/10.1016/j.commatsci.2017.04.009
90. Chau R, Stölken J, Asoka-Kumar P et al (2010) Shock hugoniot of single crystal copper. J Appl Phys. https://doi.org/10.1063/1.3283924
91. Tsai D, Beckett C (1966) Shock wave propagation in cubic lattices. J Geophys Res 71(10):2601–2608. https://doi.org/10.1029/JZ071i010p02601
92. Holian BL, Straub GK (1979) Molecular dynamics of shock waves in three-dimensional solids: transition from nonsteady to steady waves in perfect crystals and implications for the rankine-hugoniot conditions. Phys Rev Lett 43(21):1598–1600. https://doi.org/10.1103/PhysRevLett.43.1598
93. Shen T, Song H, An M et al (2022) Uncovering strengthening and softening mechanisms of nano-twinned CoCrFeCuNi high entropy alloys by molecular dynamics simulation. J Appl Phys 10(1063/5):0082835
94. Jiang J, Sun W, Luo N (2022) Molecular dynamics study of microscopic deformation mechanism and tensile properties in AlxCoCrFeNi amorphous high-entropy alloys. Mater Today Commun. https://doi.org/10.1016/j.mtcomm.2022.103861
95. Elahi S, Tavakoli R, Boukellal A et al (2022) Multiscale simulation of powder-bed fusion processing of metallic alloys. Comput Mater Sci. https://doi.org/10.1016/j.commatsci.2022.111383

96. Yan W, Huang W, Huang Q et al (2022) Data-driven multiscale method for composite plates. Comput Mech 70:1025–1040. https://doi.org/10.1007/s00466-022-02195-6
97. Xiao S, Deierling P, Attarian S et al (2021) Machine learning in multiscale modeling of spatially tailored materials with microstructure uncertainties. Comput Struct. https://doi.org/10.1016/j.compstruc.2021.106511
98. Xiong L, Deng Q, Tucker G et al (2012) A concurrent scheme for passing dislocations from atomistic to continuum domains. Acta Materialia 60(3):899–913. https://doi.org/10.1016/j.actamat.2011.11.002
99. Xiong L, Deng Q, Tucker GJ et al (2012) Coarse-grained atomistic simulations of dislocations in Al, Ni and Cu crystals. Int J Plast 38:86–101. https://doi.org/10.1016/j.ijplas.2012.05.002
100. Knap J, Ortiz M (2001) An analysis of the quasicontinuum method. J Mech Phys Solids 49(9):1899–1923. https://doi.org/10.1016/S0022-5096(01)00034-5